nature metabolism

Article

https://doi.org/10.1038/s42255-024-01115-7

Efferocytosis drives a tryptophan metabolism pathway in macrophages to promote tissue resolution

Received: 3 February 2024

Accepted: 24 July 2024

Published online: 6 September 2024

Check for updates

Santosh R. Sukka[1] ✉, Patrick B. Ampomah[1], Lancia N. F. Darville[2], David Ngai[1], Xiaobo Wang[1], George Kuriakose[1], Yuling Xiao[3], Jinjun Shi[3], John M. Koomen[2], Robert H. McCusker[4] & Ira Tabas[1,5] ✉

Macrophage efferocytosis prevents apoptotic cell (AC) accumulation and triggers inflammation-resolution pathways. The mechanisms linking efferocytosis to resolution often involve changes in macrophage metabolism, but many gaps remain in our understanding of these processes. We now report that efferocytosis triggers an indoleamine 2,3-dioxygenase-1 (IDO1)-dependent tryptophan (Trp) metabolism pathway that promotes several key resolution processes, including the induction of pro-resolving proteins, such interleukin-10, and further enhancement of efferocytosis. The process begins with upregulation of Trp transport and metabolism, and it involves subsequent activation of the aryl hydrocarbon receptor (AhR) by the Trp metabolite kynurenine (Kyn). Through these mechanisms, macrophage IDO1 and AhR contribute to a proper resolution response in several different mouse models of efferocytosis-dependent tissue repair, notably during atherosclerosis regression induced by plasma low-density lipoprotein (LDL) lowering. These findings reveal an integrated metabolism programme in macrophages that links efferocytosis to resolution, with possible therapeutic implications for non-resolving chronic inflammatory diseases, notably atherosclerosis.

The process of inflammation resolution is vital for both halting the inflammatory process and restoring tissue health and integrity[1,2]. A key process in resolution is efferocytosis, the clearance of ACs by macrophages. Efferocytosis involves the sequential processes of AC binding, mediated by certain cell-surface receptors; AC engulfment, which requires Rac1-mediated actin remodelling; and AC degradation, which occurs in acidic phagolysosomes[3]. The failure of efferocytosis contributes to diseases such as atherosclerosis, lung damage, non-alcoholic fatty liver disease, neurodegenerative disease and autoimmune disorders[4–8]. Efferocytosis not only clears dead cells to dampen necrosis and inflammation, but also triggers signalling pathways that promote resolution and tissue repair. These pathways lead to the production of resolving mediators, such as interleukin-10 (IL-10) and transforming growth factor-β1 (TGF-β1), and enhance the ability of macrophages to clear dead cells, called continuing efferocytosis, which is critical to restoring tissue health in vivo[1,2]. Accordingly, a key area of immunobiological and biomedical research is understanding how efferocytosis promotes resolution. One fascinating mechanism is

[1]Department of Medicine, Columbia University Irving Medical Center, New York, NY, USA. [2]Proteomics and Metabolomics Core, H. Lee Moffitt Cancer Center and Research Institute, Tampa, FL, USA. [3]Center for Nanomedicine and Department of Anesthesiology, Perioperative and Pain Medicine, Brigham and Women's Hospital, Harvard Medical School, Boston, MA, USA. [4]Department of Animal Sciences, Integrative Immunology and Behavior Program and Neuroscience Program, University of Illinois at Urbana-Champaign, Urbana, IL, USA. [5]Departments of Physiology and Cell Biology, Columbia University Irving Medical Center, New York, NY, USA. ✉e-mail: srs2302@columbia.edu; iat1@columbia.edu

an immunometabolic process in which efferocytosing macrophages use receptor signalling and various molecules derived from the phagolysosomal degradation of engulfed ACs to trigger metabolic pathways that activate resolving mediator synthesis and continuing efferocytosis[9–14]. However, the full extent and mechanisms of efferocytosis-induced resolution remain to be explored.

Among the amino acids delivered to macrophages following AC degradation is Trp, an essential amino acid whose metabolites downstream of the enzyme IDO1 play roles in immunity[15]. We therefore hypothesized that Trp metabolism during efferocytosis might link the process to tissue resolution. We now present evidence that expression of Trp is elevated in efferocytosing mouse and human macrophages, in a manner that is dependent on the lysosomal Trp transporter SLC36A4, which is upregulated by efferocytosis. This process results in an IDO1-dependent increase in levels of the Trp metabolite Kyn, which activates the AhR to induce the expression of pro-resolving TGF-β1 and IL-10 as well as IDO1 itself. AhR also promotes continuing efferocytosis by activating Rac1. The biochemical signature of the pathway is observed in mouse models of efferocytosis-induced resolution, and deletion of macrophage IDO1 and AhR compromises the resolution response. Notably, macrophage IDO1 knockdown during atherosclerosis regression blocks the resolution response that contributes to features of plaque stabilization. These findings define a new metabolic pathway linking efferocytosis to resolution, which can inform emerging therapeutic strategies to restore tissue homeostasis in diseases driven by defective efferocytosis and impaired resolution.

Results

Efferocytosis activates Trp metabolism in macrophages

We incubated mouse bone-marrow-derived macrophages (BMDMs) with either medium alone or medium containing ACs for 1 h, followed by incubation in medium alone ('chase') for an additional 3 h. Cell extracts were then analysed for Trp metabolites by liquid chromatography–mass spectrometry (LC–MS). There were significant increases in tryptophan (Trp) and several Trp metabolites, notably *N*-formylkynurenine, L-Kyn, kynurenic acid and quinolinic acid, in macrophages that were exposed to ACs compared with those that were not exposed to ACs, but levels of other Trp metabolites were not altered by AC exposure (Fig. 1a, Extended Data Figs. 1–3 and Supplementary Tables 1 and 2).

In efferocytosis, the macromolecules of engulfed ACs, including proteins, are hydrolysed in phagolysosomes. This is followed by transport of the hydrolysed molecules, for example, amino acids, to the macrophage cytoplasm[10,12,13]. In this context, we investigated the role of the SLC36A4 transporter, previously called proton-assisted amino acid transporter 4 (PAT4). SLC36A4 has been implicated in Trp transport in *Xenopus laevis* oocytes[16] and lysosomal amino acid pools in retinal pigment epithelial cells[17], but not in efferocytosis. To begin, we incubated control macrophages and macrophages treated with short interfering RNA targeting *Slc36a4* (si*Slc36a4*) with fluorescently labelled ACs. We then analysed the cells using immunofluorescence microscopy to detect SLC36A4 and ACs. We found that SLC36A4 colocalized with AC-containing LAMP-1$^+$ phagolysosomes; the specificity of SLC36A4 immunostaining was confirmed by the loss of signal in the si*Slc36a4*-treated macrophages (Fig. 1b and Extended Data Fig. 4a). SLC36A4 is undetectable in the ACs themselves (Extended Data Fig. 4b). Notably, macrophages incubated without ACs express very little SLC36A4 (Extended Data Fig. 4c). This observation was confirmed by a marked increase in SLC36A4 protein, detected by immunoblot, when macrophages were incubated with either apoptotic Jurkat cells or apoptotic macrophages (Fig. 1c). However, AC exposure did not lead to increased levels of *Slc36a4* mRNA in macrophages (Extended Data Fig. 4d), suggesting that efferocytosis post-transcriptionally upregulates this transporter. In terms of mechanism, upregulation of SLC36A4 was not seen in macrophages incubated with phosphatidylserine (PS)-coated beads, which bind to and are internalized by efferocytosis receptors but have no cellular cargo[18–20], indicating that neither efferocytosis receptor binding nor particle phagocytosis is sufficient to upregulate SLC36A4 (Extended Data Fig. 4e). A previous study has shown an example of efferocytosis blocking the proteasomal-mediated turnover of the Ora1 protein (ref. 21). To test the role of the proteasome in maintaining SLC36A4 at a low level in non-efferocytosing macrophages, we incubated macrophages in the basal state with the proteasomal inhibitor MG132. This treatment markedly upregulated SLC36A4, that mimicked the effect of ACs (Extended Data Fig. 4f). Most importantly, silencing SLC36A4 in efferocytosing macrophages, which did not affect primary AC engulfment itself (Extended Data Fig. 4g), lowered efferocytosis-induced increases in levels of Trp and certain Trp metabolites, including *N*-formylkynurenine, Kyn and kynurenic acid (Fig. 1d, Extended Data Fig. 4h and Supplementary Table 3).

IDO1 catalyses the first reaction in Trp metabolism, converting Trp to *N*-formylkynurenine, which is the precursor of Kyn[22]. As was the case for SLC36A4, efferocytosis upregulated IDO1, but both mRNA and protein levels were increased (groups 1 and 2 in Fig. 1e–g). Similar data were obtained when the BMDMs were incubated with apoptotic macrophages instead of apoptotic Jurkat cells (Extended Data Fig. 4i). The upregulation of *Ido1* in BMDMs was dampened by silencing SLC36A4 or by pretreating macrophages with bafilomycin A, a lysosomal vacuolar ATPase inhibitor that blocks the phagolysosomal degradation of engulfed ACs[10,23] (±ACs with siSIc36a4 treatment in Fig. 1e; ±ACs with bafilomycin treatment in Fig. 1f,g). Moreover, PS-coated beads, which have no cellular cargo (described above)[18–20], did not lead to increased *Ido1* levels (Fig. 1h). Finally, efferocytosis also upregulated *IDO1* mRNA in an SLC36A4-dependent manner in human monocyte-derived macrophages (HMDMs) (Fig. 1i and Extended Data Fig. 4j). In summary, efferocytosis leads to an increase in levels of Trp and some of its key metabolites in macrophages, accompanied by increased expression

Fig. 1 | Macrophage efferocytosis drives Trp metabolism and IDO1 expression, which are dependent on AC degradation and the amino acid transporter SLC36A4. a, Quantification of metabolite levels from BMDMs incubated with or without apoptotic Jurkat cells (ACs) for 1 h and then rinsed with PBS to remove unbound ACs. After a 3-h incubation (chase), the macrophages were subjected to LC–MS/MS analysis ($n = 6$ biological replicates per group). **b**, Immunofluorescence microscopy of SLC36A4 (green) in BMDMs that were transfected with scrambled siRNA (Scr) or si*Slc36a4* and then incubated with PKH26-labelled ACs (red) for 45 min. DAPI (blue) was used for nuclear staining. Scale bar, 50 µm. The quantified data show the MFI of SLC36A4 in AC$^+$ macrophages ($n = 3$ biological replicates per group). **c**, Immunoblot of SLC36A4 in BMDMs incubated with or without AJCs or apoptotic macrophages (Mϕ) for 1 h and then chased for 3 h. β-actin was used as a loading control. **d**, Quantification of metabolite levels from BMDMs transfected with Scr or si*Slc36a4* and then incubated with ACs ($n = 6$ biological replicates per group). **e**, BMDMs transfected with Scr or si*Slc36a4* were incubated with or without ACs for 1 h, and *Ido1* mRNA levels were assayed ($n = 3$ biological replicates per group). **f**, BMDMs pre-treated with vehicle or bafilomycin A1 (Baf) were incubated with or without ACs for 1 h and chased for 3 h, and *Ido1* mRNA levels were quantified ($n = 3$ biological replicates per group). **g**, As in **f**, with quantification of IDO1 protein by immunoblot (top), and densitometric quantification (bottom) ($n = 3$ samples per group). β-actin was used as a loading control. **h**, BMDMs were incubated with or without 10-µm phosphatidylserine (PS)-coated beads or ACs for 1 h and chased for 3 h, and *Ido1* mRNA levels were quantified ($n = 4$ biological replicates per group). n.s., not significant. **i**, HMDMs transfected with Scr or si*SLC36A4* were incubated with or without ACs and chased for 3 h, and *IDO1* mRNA levels were quantified ($n = 3$ biological replicates per group). The mRNA and densitometry data are expressed relative to the indicated control groups. Data are shown as mean ± s.e.m., and significance was determined by two-tailed Student's *t*-test or one-way analysis of variance (ANOVA) with Fisher's least significant difference (LSD) post hoc analysis.

https://doi.org/10.1038/s42255-024-01115-7

of both the Trp transporter SLC36A4 in AC-containing phagolysosomes and IDO1, suggesting a feed-forward pathway that promotes efferocytosis-induced Trp metabolism.

IDO1 licences post-efferocytic resolution in macrophages

A key process in tissue resolution is the stimulation of continuing efferocytosis after macrophages ingest and metabolize the cargo of an apoptotic cell[5,24]. We therefore asked whether IDO1 has a role in continuing efferocytosis, as would be predicted if the metabolism of Trp following the engulfment of the first AC was involved in this process. We first incubated BMDMs from WT (control) or IDO1 knockout (IDO1-KO) mice with labelled ACs for 1 h to assess primary efferocytosis. Somewhat unexpectedly, we found that primary efferocytosis was partially blunted in IDO1-KO versus control macrophages (Extended Data Fig. 5a), suggesting that IDO1 has a role in efferocytosis even before macrophages digest AC cargo. Similar data were obtained using a flow cytometry to assess the uptake of pHrodo-labelled ACs by macrophages in which levels of IDO1 were lowered using si*Ido1*

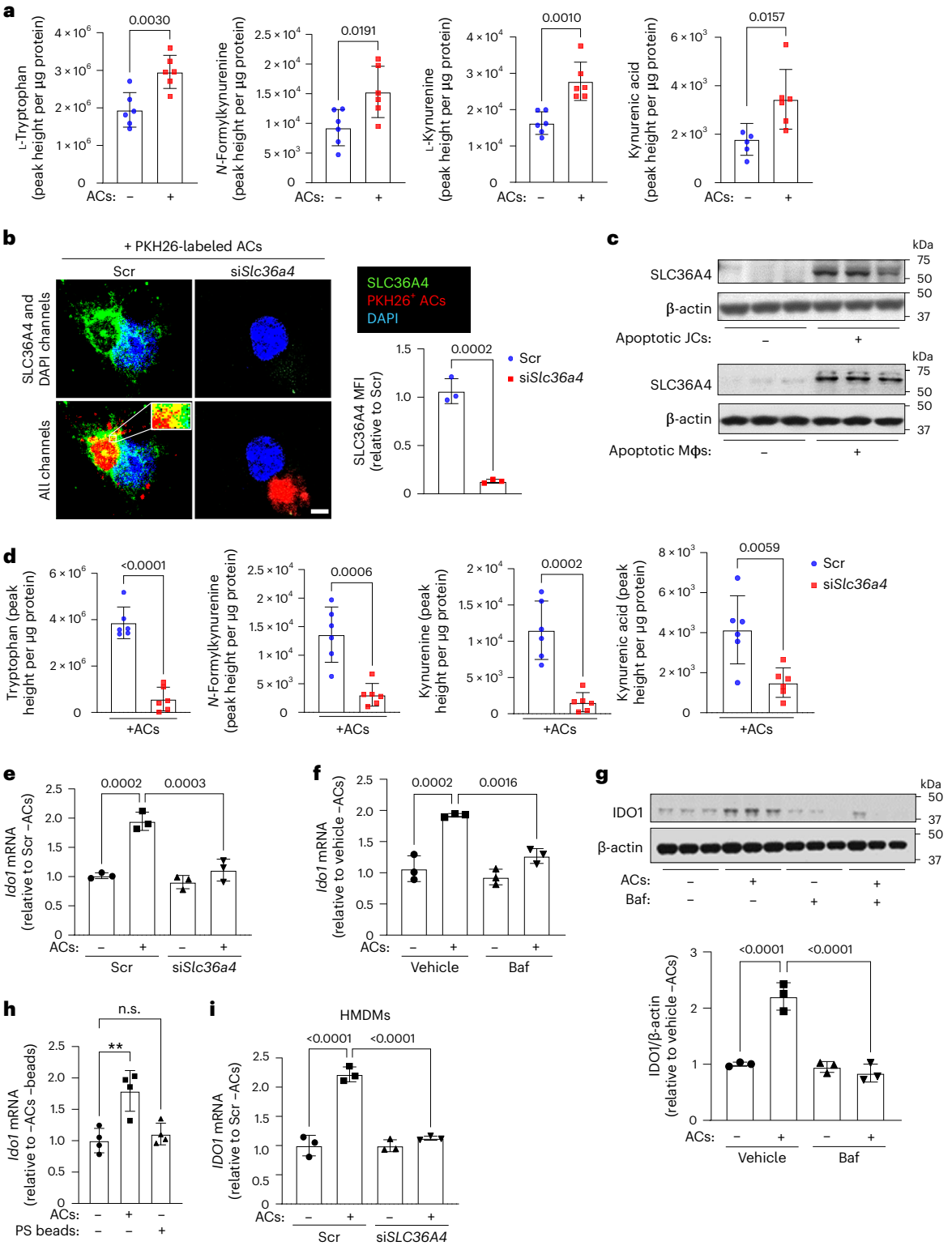

(Extended Data Fig. 5b). We then used an IDO1 inhibitor that was added after the engulfment of the first AC, to determine whether IDO1 has a role in continuing efferocytosis. To achieve this goal, we incubated BMDMs for 1 h with ACs labelled with PKH26 (red); then, after a 2-h chase in the presence of the IDO1 inhibitor epacadostat (INCB024360)[25,26] or vehicle control, we incubated the macrophages with a second round of ACs labelled with PKH67 (green). The uptake of a green AC by macrophages that had previously ingested a red AC is an indicator of continuing efferocytosis[10,24]. The IDO1 inhibitor limited uptake of the second AC by ~50% (Fig. 2a), indicating that IDO1 is necessary for maximal continuing efferocytosis. As another approach, we used flow cytometry of control versus M-IDO1-KO macrophages incubated sequentially with ACs labelled with pHrodo-red or pHrodo-green, gating on red ACs (primary efferocytosis) or red and green ACs (continuing efferocytosis) to correct for the lower number of primary efferocytosing macrophages in the IDO1-silenced macrophages. The data show a decrease in continuing efferocytosis (Fig. 2b and Extended Data Fig. 5c), confirming the findings above. IDO1 inhibition did not block binding of the second AC in the presence of cytochalasin D (Fig. 2c), indicating that IDO1 has a role in internalization of the second AC.

We next examined the effect of IDO1 KO or inhibition on Rac1 GTPase activity, because Rac1-mediated actin remodelling around the forming phagosome is a key step in the engulfment of ACs and other large substrates[27,28]. A previous study has shown a link between paxillin and Rac1 activation in the locomotion of cancer cells[29]. We therefore determined the role of IDO1 in engulfment-activated Rac1 GTPase activity using a method in which macrophages are incubated with 10-µm polystyrene beads[28]. To reflect continuing efferocytosis, bead-induced Rac1 GTPase activity was assayed in control macrophages that had been exposed to ACs and then incubated for 2 h with epacadostat versus vehicle. IDO1 inhibition suppressed post-AC bead-induced Rac1 GTPase activity (Fig. 2d), consistent with our conclusion that IDO1 contributes to the engulfment stage of continuing efferocytosis. A GTP-exchange factor needed for Rac1 activation in continuing efferocytosis is Dbl, which is upregulated by an arginase 1 (Arg1) pathway in efferocytosing macrophages[10]. In this context, treatment of macrophages with epacadostat dampened efferocytosis-induced *Arg1* and *Mcf2*, the gene that encodes Dbl1 (Extended Data Fig. 5d).

Efferocytosis stimulates the production of pro-resolving mediators, notably TGF-β1 and IL-10, which are important in tissue repair[14,30]. We found that both si*Ido1* and epacadostat markedly blocked the increases in levels of *Tgfb1* and *Il10* mRNAs in efferocytosing macrophages (Fig. 2e,f). Moreover, efferocytosis-induced increases in TGF-β1 (latency-associated peptide (LAP)-TGF-β1) protein and IL-10 protein, as assayed by flow cytometry of PKH26$^+$ (AC$^+$) and PKH26$^-$ (AC$^-$) macrophages, were partially dampened in IDO1-KO macrophages (Fig. 2g,h and Extended Data Fig. 5e,f). Thus, IDO1 in macrophages contributes to two key processes in inflammation resolution, continuing efferocytosis and efferocytosis-induced expression of TGF-β1 and IL-10. The increases in TGF-β1 and IL-10 are dependent on SLC36A4, and, as will be shown below, this is also the case for continuing efferocytosis.

Kynurenine mediates post-efferocytic resolution in macrophages

Efferocytosis increases the Trp metabolite Kyn in control macrophages but less so in macrophages lacking SLC36A4 (described above), and Kyn can activate immunosuppressive processes in other settings[31]. We therefore explored the role of Kyn in continuing efferocytosis and post-efferocytic resolution mediator induction by adding back Kyn to IDO1-inhibited, IDO1-KO or SLC36A4-silenced macrophages. Kyn was added to macrophages treated with epacadostat after the addition of the first AC, and it partially restored continuing efferocytosis (Fig. 3a). Kyn also partially restored post-efferocytic expression of *Tgfb1* and *Il10* in IDO1-KO macrophages (Fig. 3b). Similar results were observed for *TGFB1* and *IL10* in si*IDO1*-transfected HMDMs (Fig. 3c and Extended Data Fig. 5g). These data also showed that Kyn did not further enhance these endpoints in efferocytosing control macrophages. Moreover, Kyn did not boost resolution in the absence of ACs, suggesting that Kyn requires another efferocytosis-induced process ('second hit') to induce resolution, which we address in a later section. We conducted similar experiments in si*Slc36a4*-transfected macrophages. We first observed that continuing efferocytosis and efferocytosis-induced expression of *Tgfb1*, *Il10* and *Ido1* mRNA were blocked by si*Slc36a4*, consistent with a role for phagolysosomal-derived Trp in resolution signalling (Fig. 3d, bars 1 and 3; Fig. 3e, bars 1, 3, 5 and 7; and Extended Data Fig. 5h). Second, adding back Kyn to *Slc36a4*-silenced efferocytosing macrophages partially restored continuing efferocytosis and efferocytosis-induced expression of *Tgfb1*, *Il10* and *Ido1* mRNA (Fig. 3d,e). These data support the idea that Trp metabolism to Kyn in efferocytosing macrophages contributes to continuing efferocytosis and post-efferocytic resolution signalling.

We next examined the role of exogenous Trp. First, the effects of Kyn on efferocytosis-induced expression of *Tgfb1* and *Il10* in SLC36A4-silenced macrophages were not dependent upon Trp in the medium (Extended Data Fig. 5i), consistent with the idea that the Trp metabolized to pro-resolving Kyn in efferocytosing macrophages is derived from the phagolysosomal degradation of ACs rather than import of Trp from the medium. This conclusion was further supported by the finding that exogenous Trp (50 µM) added to macrophages did not increase the expression of *Tgfb1* and *Il10* and did not further increase these mRNAs in the presence of ACs (Extended Data Fig. 5j). However, exogenous Trp was able to restore resolution in si*Slc36a4*-transfected macrophages (Extended Data Fig. 5k), indicating that macrophages can use an alternative source of Trp when Trp derived from degraded ACs is blocked and if the concentration in the medium is high enough.

Mice lacking myeloid IDO1 have impaired resolution in vivo

As an initial step to investigate the relevance of the above findings to resolution in vivo, we collected peritoneal macrophages from C57BL/6J mice 24 h after intraperitoneal (i.p.) injection with 1 mg of the yeast cell-wall component zymosan A or PBS control. In this model, zymosan-induced sterile inflammation triggers the recruitment of polymorphonuclear cells (PMNs), which peaks at 12 h, followed by PMN apoptosis. The apoptotic PMNs are then cleared by peritoneal macrophages, which promotes a resolution response[10,13,32]. We found that exudate macrophages analysed from mice 24 h after zymosan injection had higher IDO1 expression than did macrophages from PBS-injected mice (Fig. 4a). We then conducted a zymosan experiment in irradiated mice transplanted with BM from M-IDO1-KO (*Ido1*$^{fl/fl}$*Lyz2cre*$^{+/-}$) or control (*Lyz2cre*$^{+/-}$) mice and found that the PMN counts were significantly higher in the M-IDO1-KO animals (Fig. 4b). To determine whether this difference might be due to impaired efferocytosis in the M-IDO1-KO cohort, we used flow cytometry to quantify the percentage of exudate F4/80$^+$ macrophages that internalized Ly6G$^+$ PMNs[10,13]. As expected[10,13], efferocytosis was increased 24 h after zymosan treatment in the control mice, but this increase was significantly blunted in the M-IDO1-KO mice (Fig. 4c). Zymosan-induced efferocytosis in this model induces the synthesis of pro-resolving mediators, notably TGF-β1 and IL-10, at 24 h, and the zymosan-induced increases in the concentrations of these proteins in peritoneal exudates were also significantly blunted in the M-IDO1-KO cohort (Fig. 4d). Thus, IDO1 is necessary for a full resolution response in the zymosan model of sterile inflammation.

We next turned to another in vivo model of efferocytosis-induced resolution in which thymocyte apoptosis is induced by dexamethasone. This is followed by efferocytosis of apoptotic thymocytes by thymic macrophages, which is necessary to prevent thymic necrosis[10,12,13]. We applied this model to control- and M-IDO1-KO-transplanted mice (above), and we included additional cohorts in which Kyn was administered (100 mg kg^{-1} i.p., followed by 5 mM in the drinking water) at the

https://doi.org/10.1038/s42255-024-01115-7

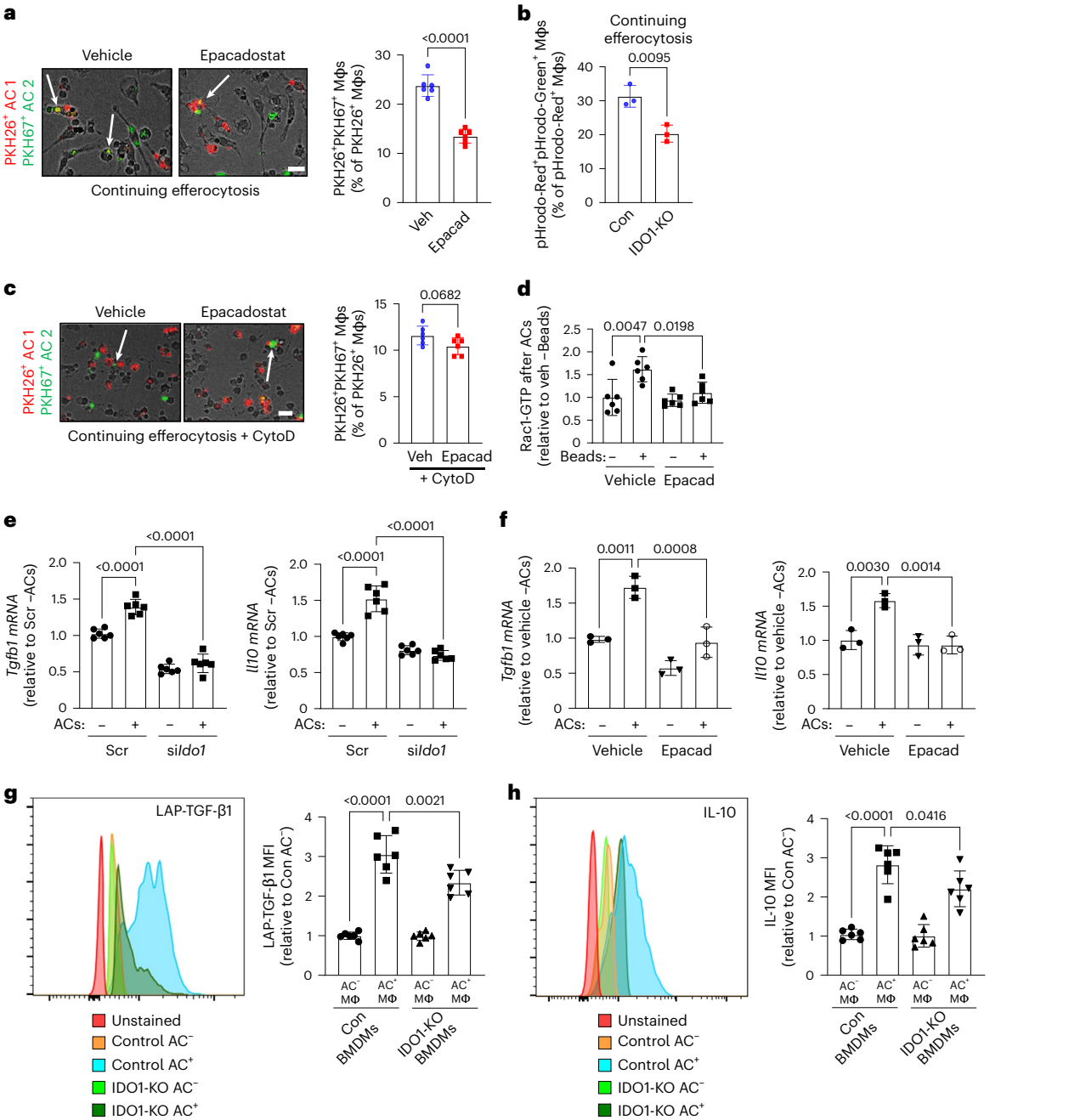

Fig. 2 | IDO1 deficiency or inhibition suppresses continuing efferocytosis and post-efferocytic resolving mediator induction. a, To assess the role of IDO1 in continuing efferocytosis, BMDMs were incubated with PKH26-labelled ACs (red) and then treated with vehicle (Veh) or epacadostat (200 nM) (Epacad), followed by incubation with PKH67-labelled ACs (green). The percentage of $PKH26^+PKH67^+$ macrophages among the $PKH26^+$ macrophages was then quantified. Arrows, $PKH26^+PKH67^+$ macrophages. Scale bar, 50 µm ($n = 6$ biological replicates per group). **b**, Control (Con) or IDO1-KO BMDMs were incubated with pHrodo-Red-labelled ACs, followed by incubation with pHrodo-green-labelled ACs. The cells were then analysed by flow cytometry, gating on pHrodo-red$^+$ (AC^+) and pHrodo-red$^-$ (AC^-) macrophages (Extended Data Fig. 5c). The percentage of pHrodo-Red$^+$pHrodo-Green$^+$ macrophages among the pHrodo-Red$^+$ macrophages was quantified ($n = 3$ biological replicates per group). **c**, As in **a**, but the cohorts was also treated with 10 µM cytochalasin D (CytoD) before the second round of efferocytosis to assess second-AC binding. Arrows, $PKH26^+PKH67^+$ macrophages. Scale bar, 50 µm ($n = 6$ biological replicates per group). **d**, BMDMs were incubated with ACs and then treated with vehicle or epacadostat, followed 2 h later by incubation with or without 10-µm polystyrene beads for 20 min and measurement of GTP-bound Rac1 ($n = 6$ biological replicates per group). **e**, Scr- or si*Ido1*-transfected BMDMs were incubated with or without ACs for 1 h. After a 6-h chase, levels of *Tgfb1* and *Il10* mRNA were quantified ($n = 6$ biological replicates per group). **f**, As in **e**, but the cells were incubated with or without epacadostat during the 6-h chase period ($n = 3$ biological replicates per group). **g**,**h**, Control or IDO1-KO BMDMs were incubated with PKH26-labelled ACs for 1 h, followed by an additional 18 h of incubation. The MFIs of TGF-β1 and IL-10 were analysed using flow cytometry, gating on $PKH26^+$ (AC^+) and $PKH26^-$ (AC^-) macrophages ($n = 6$ biological replicates per group). The mRNA data are expressed relative to the indicated control groups. Data are mean ± s.e.m., and significance was determined by two-tailed Student's *t*-test or one-way ANOVA with Fisher's LSD post hoc analysis.

https://doi.org/10.1038/s42255-024-01115-7

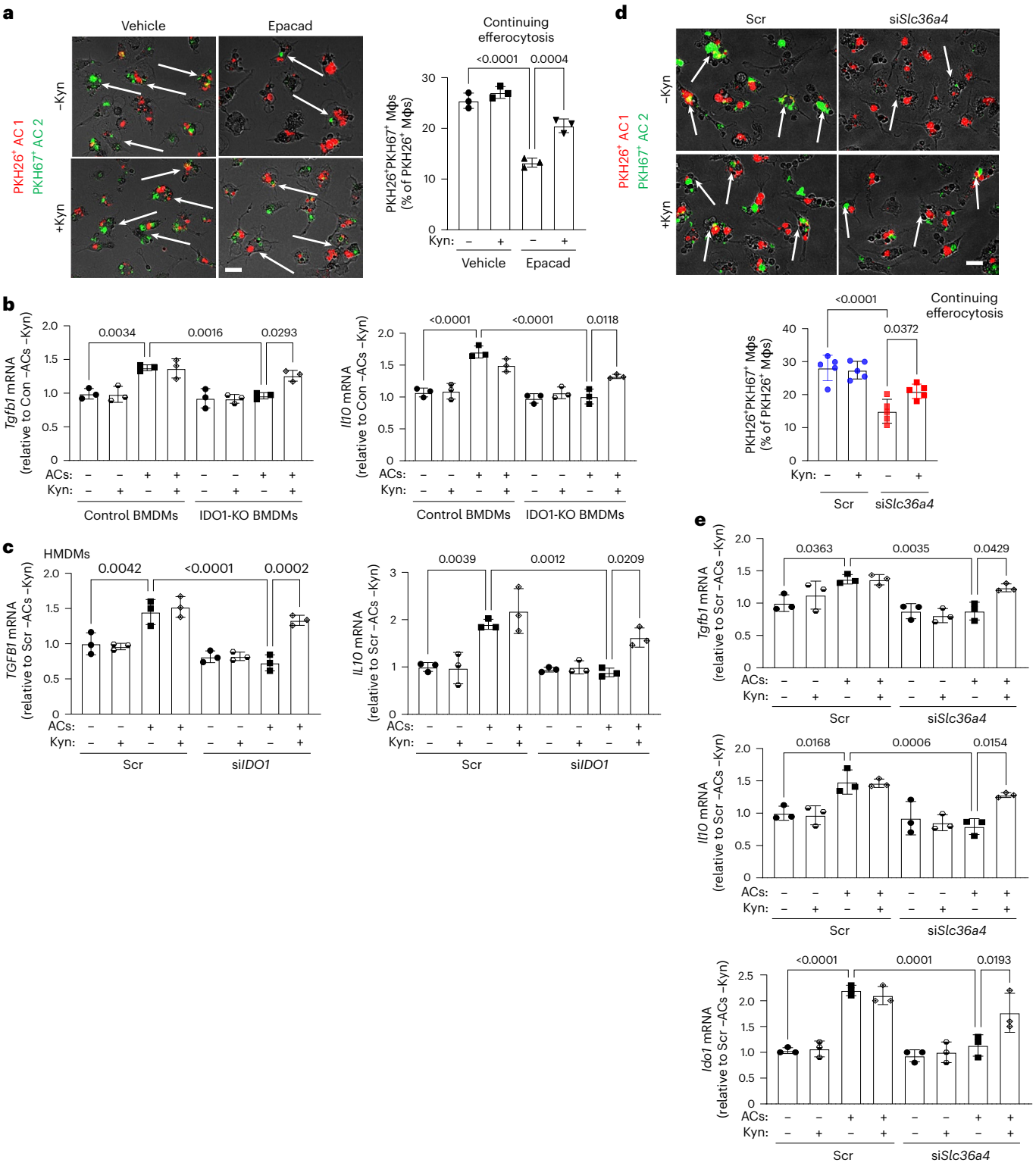

Fig. 3 | Continuing efferocytosis and resolving mediator induction require SLC36A4 and the Trp metabolite Kyn. a, BMDMs were incubated with PKH26-labelled ACs (red) and then treated with vehicle or epacadostat with or without Kyn (50 µM), followed by incubation with PKH67-labelled ACs (green). The percentage of PKH26$^+$PKH67$^+$ macrophages among PKH26$^+$ macrophages was quantified. Arrows, PKH26$^+$PKH67$^+$ macrophages. Scale bar, 50 µm ($n = 3$ biological replicates per group). **b**, Control or IDO1-KO BMDMs were pre-treated for 1 h with vehicle or Kyn and then incubated with or without ACs and chased for 6 h, and *Tgfb1* and *Il10* mRNA levels were quantified ($n = 3$ biological replicates per group). **c**, HMDMs transfected with Scr or si*IDO1* were pre-treated with vehicle or Kyn for 1 h and then incubated with or without ACs for 1 h. After a 6-h chase, levels of *TGFB1* and *IL10* mRNA were analysed ($n = 3$ biological replicates per group). **d**, Macrophages were assayed for continuing efferocytosis as in **a**, but were transfected with Scr or si*Slc36a4* and pre-treated for 1 h with vehicle or Kyn. Arrows, PKH26$^+$PKH67$^+$ macrophages. Scale bar, 50 µm ($n = 5$ biological replicates per group). **e**, BMDMs transfected with Scr or si*Slc36a4* were pre-treated with vehicle or Kyn for 1 h and then incubated with or without ACs for 1 h. After a 6-h chase, levels of *Tgfb1* and *Il10* mRNA were analysed, and *Ido1* mRNA levels were analysed after a 3-h chase ($n = 3$ biological replicates per group). The mRNA data are expressed relative to the indicated control groups. The data are mean ± s.e.m., and significance was determined by two-tailed Student's *t*-test or one-way ANOVA with Fisher's LSD post hoc analysis.

time of dexamethasone injection. For all groups, the thymi were analysed 24 h after dexamethasone injection. First, to assess the relevance of efferocytosis-induced upregulation of IDO1 and SLC36A4 in vivo, we assayed their expression in efferocytosing versus non-efferocytosing thymic macrophages in post-dexamethasone thymi of the control mice. Efferocytosing macrophages are identified by the presence of cytoplasmic TUNEL[10,12,13]. The immunofluorescence data showed that the expressions of both IDO1 and SLC36A4 were higher in efferocytosing versus non-efferocytosing macrophages (Fig. 4e). Next, moving to the comparison of the control and M-IDO1-KO groups, IDO1 expression in thymic macrophages was much lower in M-IDO1-KO mice than in control mice (Extended Data Fig. 6a). Thymus weight, and thymus cellularity in particular, were increased in the M-IDO1-KO cohort, which is a marker of impaired efferocytosis and resolution, and Kyn supplementation in the M-IDO1-KO mice normalized these parameters (Extended Data Fig. 6b). Most notably, the M-IDO1-KO cohort showed evidence of defective efferocytosis by thymic macrophages, that is an increase in annexin V$^+$ apoptotic cells (Fig. 4f), which was accompanied by a lower ratio of macrophage-associated to free TUNEL$^+$ cells. This was normalized by Kyn supplementation (Fig. 4g, top row of images and graph). The decrease in efferocytosis in M-IDO1-KO thymi was not associated with a change in thymic macrophages (Extended Data Fig. 6c). The M-IDO1-KO thymi also had lower levels of TGF-β1 and IL-10 immunofluorescence in macrophage-rich areas, which was normalized in the Kyn-treated group (Fig. 4g, second and third rows of images and graphs). Finally, thymic necrosis was worse in the M-IDO1-KO group and was corrected by Kyn administration (Fig. 4g, fourth row of images and graph). These combined data provide in vivo evidence for the pro-resolving role of macrophage IDO1 and Kyn in settings of efferocytosis-induced resolution.

The aryl hydrocarbon receptor mediates post-efferocytic resolution

The AhR functions as a receptor for Trp metabolic products, including Kyn, to mediate immunosuppression, tolerance and immunity[33–37]. We therefore hypothesized that resolution by the efferocytosis-mediated Trp–Kyn pathway might involve AhR. AhR activation is marked by its translocation from the cytosol to the nucleus[38]; we found that incubation of macrophages with ACs increased the expression of nuclear AhR protein while lowering levels of cytosolic AhR (Fig. 5a, lanes 1–6). Moreover, these changes were blocked by epacadostat, consistent with dependence on IDO1 (Fig. 5a, lanes 7–12). As further evidence for efferocytosis-induced AhR activation, we assayed two mRNAs induced by nuclear (active) AhR, *Cyp1a1* and *Cyp1b1*, and found that the levels of both mRNAs were increased in macrophages exposed to ACs (bar 3 versus 1 in Fig. 5b and bars 1–4 in Extended Data Fig. 6d). *Cyp1a1* was also increased in BMDMs incubated with apoptotic macrophages instead of apoptotic Jurkat cells (Extended Data Fig. 6e). The increases in *Cyp1a1* and *Cyp1b1* levels were blocked by IDO1 KO or si*Slc36a4* and partially restored by Kyn (bars 5–8 in Fig. 5b and Extended Data Fig. 6d). As was the case with the induction of resolution mRNAs (above), Kyn alone did not lead to increased levels of *Cyp1a1* and *Cyp1b1*, consistent with the idea that a 'second hit' is required for Kyn-dependent AhR activation (below). ACs also increased *CYP1A1* and *CYP1B1* in HMDMs in an SLC36A4-dependent manner (Extended Data Fig. 6f).

To test causation, we used AhR KO macrophages (BMDMs from *Ahr*$^{-/-}$ mice) or AhR-silenced macrophages. In contrast to the situation with IDO1, AhR was not required for primary efferocytosis (Extended Data Fig. 6g). We found that continuing efferocytosis was decreased by both deletion of AhR and inhibition of AhR activity using CH223191 (ref. 39) (Fig. 5c and Extended Data Fig. 6h). Moreover, as was the case with silencing *Ido1* and *Slc36a4*, the defect in continuing efferocytosis in AhR-inhibited macrophages was not due to decreased AC binding, that is binding in the presence of cytochalasin D was not affected by AhR inhibition (Extended Data Fig. 6i). This finding supports the idea that the Trp–Kyn pathway in efferocytosing macrophages promotes second-AC internalization. Silencing the AhR gene also decreased efferocytosis-induced *Tgfb1*, *Il10* and *Ido1* mRNA expression (Fig. 5d and Extended Data Fig. 6j), and we obtained similar results for *TGFB1*, *IL10* and *IDO1* mRNA expression in HMDMs (Fig. 5e and Extended Data Fig. 6k). Previous work has shown that expression of *Ido1* mRNA can be induced by AhR[40]. The transcriptional activity of AhR depends on its interaction with aryl hydrocarbon receptor nuclear translocator (ARNT)[41]. Accordingly, silencing ARNT dampened efferocytosis-induced expression of *Tgfb1*, *Il10* and *Ido1* mRNA (Fig. 5f and Extended Data Fig. 6l). Notably, the decreases in continuing efferocytosis and AC-induced induction of *Tgfb1*, *Il10* or *Ido1* mRNA expression with AhR inhibition could not be rescued by Kyn (Fig. 5g,h), supporting the conclusion that Kyn promotes resolution by activating AhR and that Kyn is upstream of AhR. These data point to the importance of efferocytosis-induced Kyn expression as a requirement for AhR activation and subsequent continuing efferocytosis and resolution signalling.

Kynurenine and ERK activate AhR in efferocytic macrophages

As noted, Kyn alone did not boost AhR activation or resolution in the absence of ACs, suggesting that Kyn requires another efferocytosis-induced process (second hit) for these actions. Given that two previously reported AC-cargo resolution pathways required efferocytic receptor-mediated ERK1/2 activation[12,13], we asked whether the combination of Kyn and PS-coated beads, which activate certain efferocytosis receptors[19,20,42], could enhance AhR activation and resolution signalling. For this purpose, we assayed *Cyp1a1* induction and nuclear AhR for AhR activation and *Il10* and *Tgfb1* mRNA levels as markers of resolution. We found that, although neither Kyn alone nor PS beads alone could activate AhR or induce *Ido1*, *Il10*, or *Tgfb1* mRNA expression, the combination of Kyn and PS beads was able to activate these downstream mediators (Fig. 6a and Extended Data Fig. 7a, b). Similar data for AhR activation and *Il10* mRNA expression were obtained using exogenous Trp (50 μM) instead of Kyn, and supported the finding that exogenous

Fig. 4 | Role of IDO1 and Kyn in resolution in vivo. a, Mice were injected i.p. with PBS or zymosan A1 (Zymo). After 24 h, peritoneal exudates were assayed by flow cytometry for the MFI of IDO1 in F4/80$^+$ cells (n = 5 mice per group). **b**–**d**, Mice were transplanted with bone marrow from *Lyz2cre*$^{+/-}$ (control) or *Ido1*$^{fl/fl}$*Lyz2cre*$^{+/-}$ (M-IDO1-KO) mice, which was followed 4 weeks later by injection with PBS or zymosan A1. After 24 h, the peritoneal exudate cells were assayed by flow cytometry for Ly6G$^+$ polymorphonuclear leukocytes (PMNs) and for the percentage of F4/80$^+$ macrophages (Mφs) that were Ly6G$^+$ (efferocytosis of neutrophils), and by ELISA for TGF-β1 and IL-10 (n = 5 mice per group). **e**–**g**, Control and M-IDO1-KO BMT mice were injected with dexamethasone, and some were then supplemented with Kyn (100 mg kg^{-1} i.p. and 5 mM in the drinking water). After 18 h, thymi were collected (n = 8 mice per group). **e**, Thymi from dexamethasone (Dex)-treated control mice were immunostained for IDO1 (left) and SLC36A4 (right), which were pseudocoloured white, and efferocytosing macrophages were identified by co-localization of TUNEL stain (red) with Mac2 (macrophages; green). The MFIs for IDO1 and SLC36A4 in efferocytosing (TUNEL$^+$) and non-efferocytosing (TUNEL$^-$) macrophages were quantified. Scale bars, 50 μm. Arrows, examples of colocalization of IDO1 and SLC36A4 with efferocytosing TUNEL$^+$ macrophages. **f**, Quantification of annexin V$^+$ (apoptotic) cells in the thymus that were assayed by flow cytometry. **g**, The first three rows of images show examples of immunostaining for Mac2 (macrophages; green) together with staining for TUNEL$^+$ cells (red) to analyse efferocytosis (row 1), TGF-β1 (red; row 2) and IL-10 (red; row 3). Scale bar, 50 μm. The fourth row of images shows areas of thymic necrosis. Scale bar, 200 μm. Arrows, examples of colocalization of TUNEL, TGF-β1 or IL-10 with Mac2$^+$ cells. The graphs show the quantification of these data. Data are shown as mean ± s.e.m., and significance was determined by one-way ANOVA with Fisher's LSD post hoc analysis.

https://doi.org/10.1038/s42255-024-01115-7

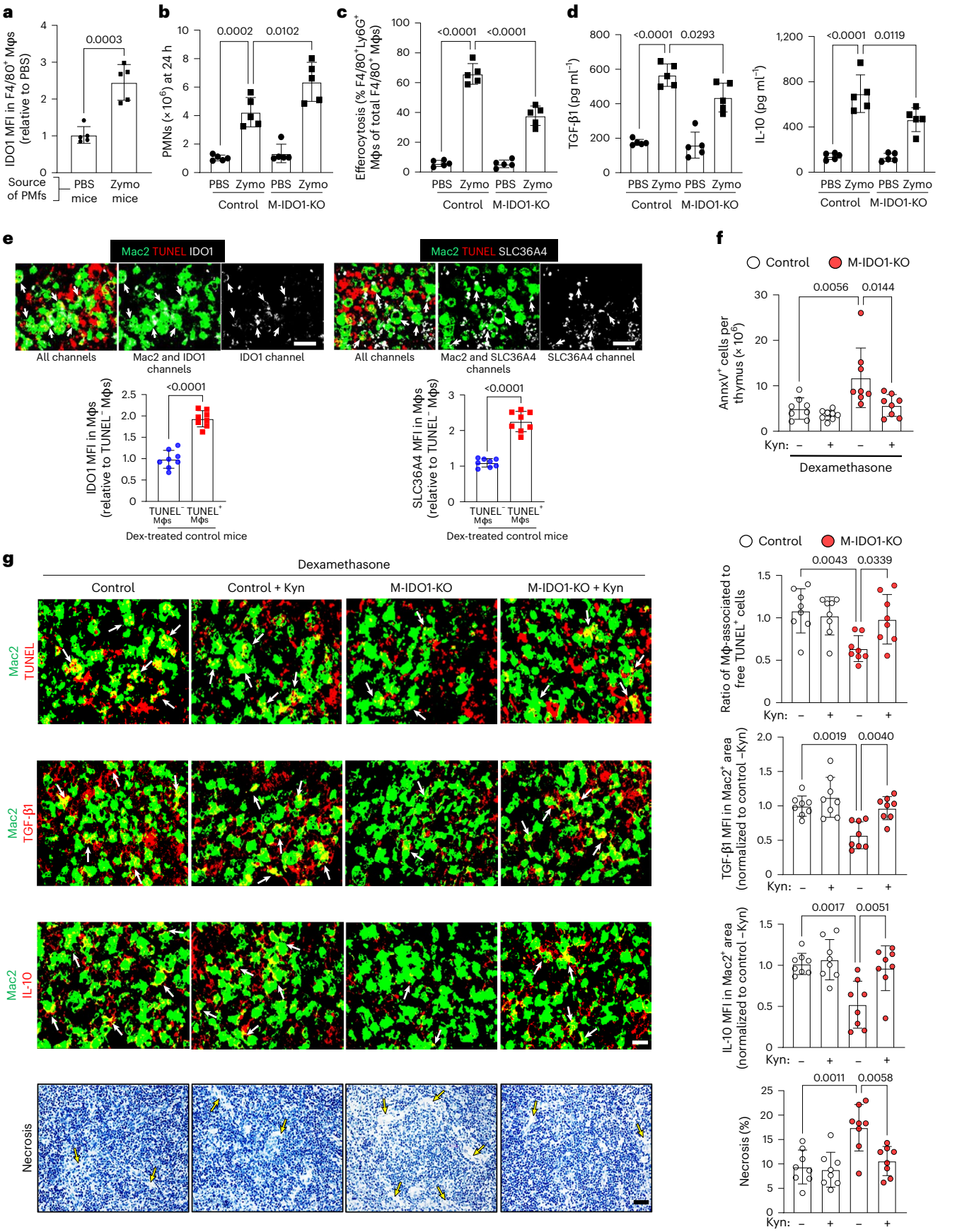

https://doi.org/10.1038/s42255-024-01115-7

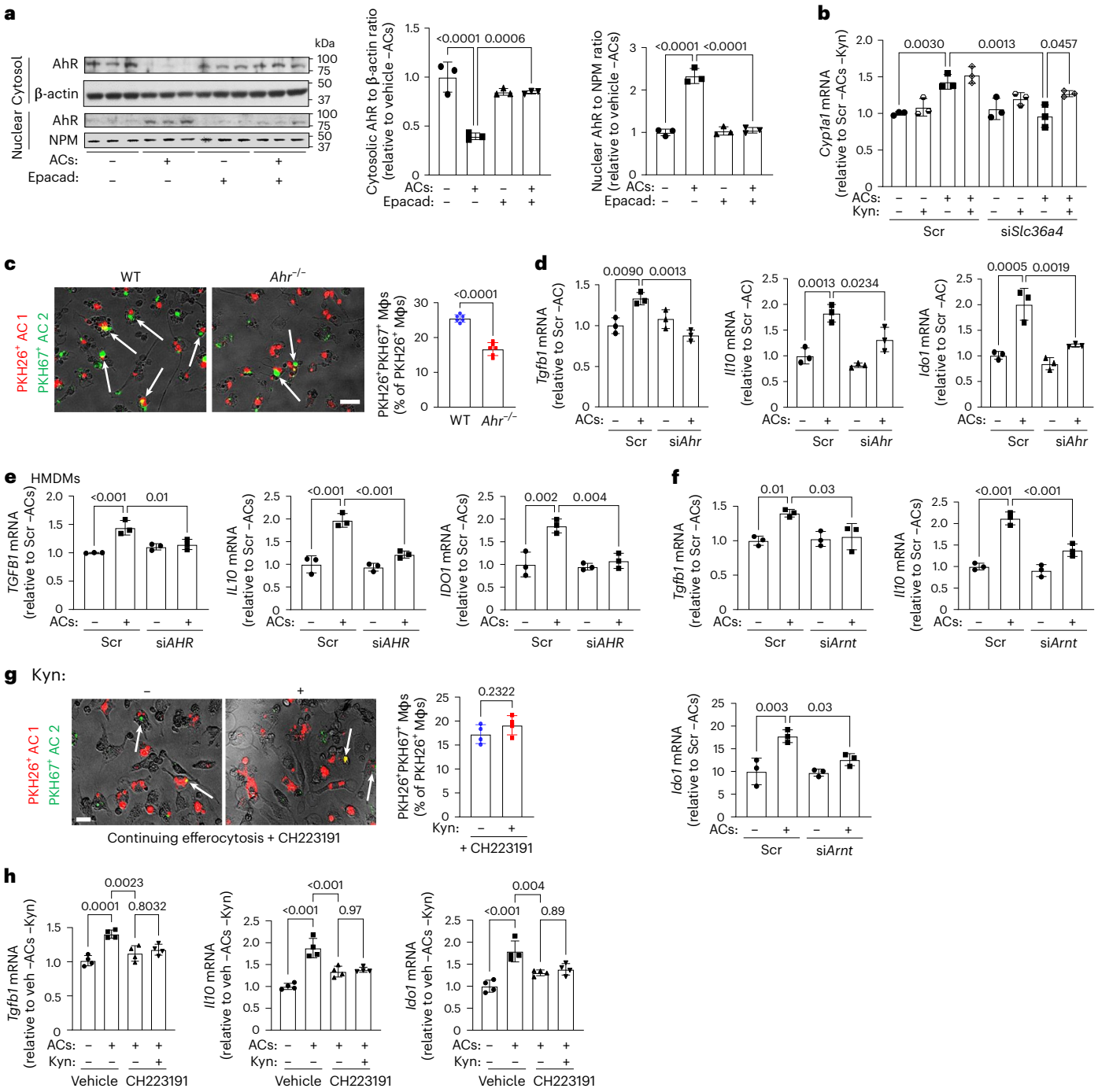

Fig. 5 | AC-derived Kyn induces *Tgfb1* and *Il10* expression and promotes continuing efferocytosis through an AhR pathway. a, BMDMs incubated with or without ACs and chased for 3 h with vehicle or epacadostat were assayed for AhR in nuclear and cytoplasmic extracts, with β-actin and nucleophosmin (NPM) as loading controls ($n = 3$ samples per group). **b**, Scr- or si*Slc36a4*-transfected BMDMs were pre-treated for 1 h with vehicle or Kyn and then incubated with or without ACs for 1 h. After a 6-h chase, *Cyp1a1* mRNA levels were analysed ($n = 3$ biological replicates per group). **c**, WT or *Ahr*$^{-/-}$ macrophages were assayed for continuing efferocytosis, as in Figure 2a. Arrows, PKH26^{+}PKH67^{+} macrophages. Scale bar, 50 µm ($n = 6$ biological replicates per group). **d**, Scr- or si*AhR*-transfected BMDMs were incubated with or without ACs for 1 h. *Ido1* mRNA levels were analysed after a 3-h chase, and *Tgfb1* and *Il10* mRNA levels were analysed after a 6-h chase ($n = 3$ biological replicates per group). **e**, Scr- or si*AHR*-transfected HMDMs were incubated with or without ACs for 1 h. *IDO1* mRNA levels were analysed after a 3-h chase, and *TGFB1* and *IL10* mRNA levels were analysed after a 6-h chase ($n = 3$ biological replicates per group). **f**, Scr- or si*Arnt*-transfected BMDMs were incubated with or without ACs for 1 h. *Ido1* mRNA levels were analysed after a 3-h chase, and *Tgfb1* and *Il10* mRNA levels were analysed after a 6-h chase ($n = 3$ biological replicates per group). **g**, BMDMs were pre-treated with CH223191 with or without Kyn for 1 h and then assayed for continuing efferocytosis, as in Figure 2a. Arrows, PKH26^{+}PKH67^{+} macrophages. Scale bar, 50 µm ($n = 4$ biological replicates per group). **h**, BMDMs were pre-treated with vehicle or Kyn with or without CH223191 for 1 h and were incubated with or without ACs for 1 h. After a 6-h chase, *Tgfb1* and *Il10* mRNA levels were analysed, and *Ido1* mRNA levels were analysed after a 3-h chase ($n = 4$ biological replicates per group). The mRNA data are expressed relative to the indicated control groups. Data are shown as mean ± s.e.m., and significance was determined by two-tailed Student's *t*-test or one-way ANOVA with Fisher's LSD post hoc analysis.

Trp alone was ineffective (Extended Data Fig. 7c). This result, which is consistent with the data shown in Extended Data Figure 5k, indicates that macrophages can use an alternative source of Trp if Trp from ACs is not available. To establish a link to ERK, we first verified our previous data[12,13] that incubation of macrophages with ACs activates (phosphorylates) ERK1 and ERK2 (ERK1/2) (Fig. 6b, lanes 1–4) and then showed that PS beads alone or Kyn alone caused only slight ERK1/2 activation, but the combination caused a more robust increase in phosphorylated ERK1/2 (Fig. 6b, lanes 5–10). Most importantly, inhibition of ERK1/2 by U0126 (ref. 43), a selective inhibitor of MEK and ERK, blocked the efferocytosis-induced increases in nuclear AhR (Fig. 6c) and AhR–ARNT interaction[41] without affecting total AhR or ARNT levels in the cell lysate (Fig. 6d and Extended Data Fig. 7d). U0126 also blocked the increases in *Il10*, *Tgfb1* and *Ido1* mRNA expression caused by PS beads plus Kyn and by efferocytosis (Fig. 6e and Extended Data Fig. 7e).

AhR forms a complex with HSP90 and XAP2, which anchors AhR in the cytoplasm when no ligand is present, safeguards it from degradation along with another protein called P23 and maintains AhR's high-affinity ligand-binding state[44,45]. Thus, these proteins are critical for subsequent AhR ligand-induced nuclear translocation and activation when an AhR ligand is present. We therefore questioned whether the combination of PS beads and Kyn might upregulate expression of the mRNAs for these proteins. The data show that the combination of PS beads and Kyn, but not either alone, upregulates *Hsp90* and *Xap2*, but not *P23* (Fig. 6f). Incubation of macrophages with ACs also upregulated *Hsp90* and *Xap2* (Fig. 6g), and HSP90 upregulation was also observed in HMDMs (Fig. 6h). Further, ERK inhibition blocked the increases in levels of these mRNAs in macrophages incubated with either PS beads and Kyn or ACs (Fig. 6i,j). Consistent with the idea that these processes are upstream of AhR activation, the increase in *Hsp90* and *Xap2* in efferocytosing macrophages was not blocked by the AhR antagonist CH223191 (Extended Data Fig. 7f). Most importantly, partial silencing of Hsp90 or Xap2 blocked the ability of ACs to increase *Il10* mRNA, nuclear AhR, and, for si*Hsp90*, continuing efferocytosis (Fig. 6k–m) without affecting primary efferocytosis (Extended Data Fig. 7g). These data support the idea of a two-hit model in which the combination of AC-induced ERK activation and an AC-mediated increase in cellular Kyn promote nuclear AhR and AhR-mediated resolution signalling (Extended Data Fig. 7h).

Myeloid AhR deletion impairs resolution in vivo

To assess the role of AhR in vivo, we transplanted mice with bone marrow from $Ahr^{fl/fl}Lyz2cre^{+/-}$ (M-AhR-KO) or control ($Lyz2cre^{+/-}$) mice and then conducted the dexamethasone–thymus protocol (described above). As designed, AhR was deleted in thymic macrophages in the M-AhR-KO cohort (Extended Data Fig. 7i). Although thymic weights were similar (Extended Data Fig. 7j), the M-AhR-KO thymi had higher cellularity (Fig. 7a) and, most importantly, an increase in the number of apoptotic cells (Fig. 7b) and a decreased ratio of macrophage-associated to free TUNEL$^+$ cells (Fig. 7c), indicative of impaired continuing efferocytosis. These differences were observed despite there being no difference in the number of F4/80$^+$ thymic macrophages between the two cohorts (Extended Data Fig. 7k). We then used IFM to examine the AhR-pro-resolving mediator pathway. The mean fluorescence intensity (MFI) values for TGF-β1, IL-10 and IDO1 were lower in Mac2$^+$ thymic macrophages of M-AhR-KO versus control mice (Fig. 7d). Finally, consistent with the defects in efferocytosis and resolution, the thymi of the M-AhR-KO cohort had a higher level of thymic necrosis than did the control thymi (Fig. 7e). These combined data support the role of the AhR tissue-resolution pathway in a high efferocytosis setting in vivo.

Macrophage IDO1 deletion impairs atherosclerosis regression

In people with atherosclerosis, marked lowering of plasma low-density lipoprotein (LDL) leads to changes in plaque morphology, notable thickening of the fibrous cap and a decrease in lesional necrosis, which are associated with a decreased risk for acute atherothrombotic events, notably myocardial infarction[46,47]. These changes in plaque morphology can be modelled in Western diet (WD)-fed $Ldlr^{-/-}$ following marked cholesterol reduction[10,48], for example by genetically restoring hepatic LDL receptors using a non-integrating helper-dependent adenovirus (HDAd-LDLR) and switching to a chow diet. Notably, regression after LDL lowering is associated with a burst of efferocytosis and tissue resolution signalling mediated by regressing plaque macrophages, both of which are required for regression[10,48]. To test the role of macrophage IDO1 (Mϕ-IDO1) in plaque regression, we transplanted $Ldlr^{-/-}$ mice with bone marrow from $Ido1^{fl/fl}Cx3cr1cre^{ERT2+/-}$ mice, which allows inducible deletion of IDO1 in macrophages upon tamoxifen (TAM) treatment (Mϕ-IDO1-iKO). The control group consisted of mice transplanted with $Ido1^{fl/fl}$ bone marrow. Two cohorts each of iKO and control mice were fed the WD for 16 weeks, after which one cohort of each genotype was harvested (baseline). The other control and Mac-IDO1-iKO mice were switched to a chow diet and injected with HDAd-LDLR and treated with TAM, and their cells were collected 7 weeks later.

Body weight, plasma cholesterol and blood glucose, as well as numbers of blood leukocytes, neutrophils, lymphocytes, monocytes, eosinophils, basophils, red blood cells and platelets, were similar between the control and Mϕ-IDO1-iKO groups in both progression and regression (Extended Data Fig. 8a–k). We began by assessing the expression of IDO1 and SLC36A4 in efferocytosing versus non-efferocytosing macrophages in the regressing lesions of control mice. Similar to the findings in the dexamethasone–thymus experiment, expression levels of both IDO1 and SLC36A4 were higher in efferocytosing macrophages (Fig. 8a,b). Next, we documented the deletion of IDO1 in lesional macrophages in the Mϕ-IDO1-iKO cohort in the regression

Fig. 6 | Kyn requires ERK1/2 for AhR activation and resolution signalling in efferocytic macrophages. a, BMDMs were incubated for 1 h with ACs, 100 μM Kyn or control (non-PS) or PS beads (PS) with or without Kyn, and nuclear AhR levels was analysed after a 3-h chase and *Il10* mRNA levels were analysed after a 6-h chase ($n = 4$ samples per group). **b**, BMDMs incubated with ACs, PS, Kyn or PS and Kyn were immunoblotted for phosphorylated ERK1/2 (p-ERK1/2), total ERK1/2 and β-actin as a loading control ($n = 4$ samples per group). **c**, BMDMs pre-treated with vehicle or the MEK and ERK inhibitor U0126 were incubated with or without ACs and immunoblotted for nuclear AhR after a 3-h chase ($n = 3$ samples per group). **d**, BMDMs were pre-treated with U0126 or were not pre-treated, and were incubated with ACs and immunoprecipitated (IP) with anti-ARNT antibody or control IgG after a 3-h chase. The immunoprecipitate was immunoblotted for AhR and ARNT (input) ($n = 3$ samples per group). **e**, BMDMs were treated with PS and Kyn with or without U0126 (top) or ACs with or without U0126 (bottom) for 1 h, and *Il10* mRNA levels were analysed after a 3-h chase ($n = 3$ biological replicates per group). **f**, BMDMs were incubated with PS, Kyn or both, and *Hsp90*, *Xap2* or *P23* mRNA levels were analysed after a 3-h chase ($n = 4$ biological replicates per group). **g**, BMDMs were incubated with or without ACs, and *Hsp90* or *Xap2* mRNA levels were analysed after a 3-h chase ($n = 3$ biological replicates per group). **h**, HMDMs were incubated with or without ACs, and *HSP90* mRNA levels were analysed after a 3-h chase ($n = 3$ biological replicates per group). **i**, BMDMs were incubated with PS and Kyn with or without U0126 for 1 h, and *Hsp90* or *Xap2* mRNA levels were analysed after a 3-h chase ($n = 3$ biological replicates per group). **j**, BMDMs were incubated with or without ACs and with or without U0126 for 1 h, and *Hsp90* or *Xap2* mRNA levels were analysed after a 3-h chase ($n = 3$ biological replicates per group). **k**,**l**, BMDMs were treated with Scr, si*Hsp90* or si*Xap2* and incubated with or without ACs, and *Il10* mRNA levels were analysed after a 6-h chase, and nuclear AhR levels were analysed after a 3-h chase ($n = 3$ samples per group). **m**, Scr- or si*Hsp90*-transfected BMDMs were assayed for continuing efferocytosis, as in Figure 2a. Arrows, PKH26$^+$PKH67$^+$ macrophages. Scale bar, 50 μm ($n = 3$ biological replicates per group). The mRNA data are expressed relative to the indicated control groups. Data are shown as mean ± s.e.m., and significance was determined by two-tailed Student's *t*-test for **d** and **g** or one-way ANOVA with Fisher's LSD post hoc analysis for the other panels.

https://doi.org/10.1038/s42255-024-01115-7

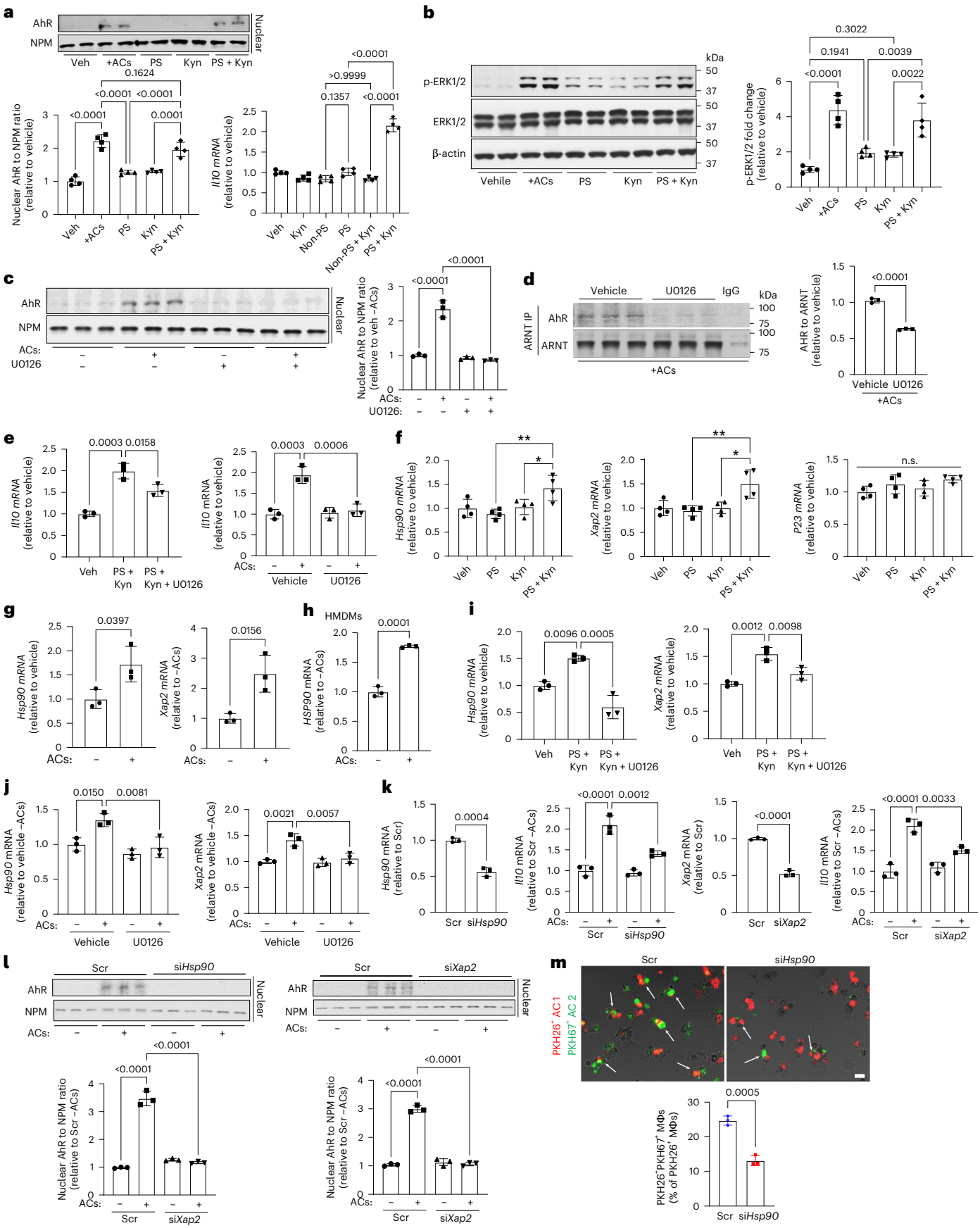

https://doi.org/10.1038/s42255-024-01115-7

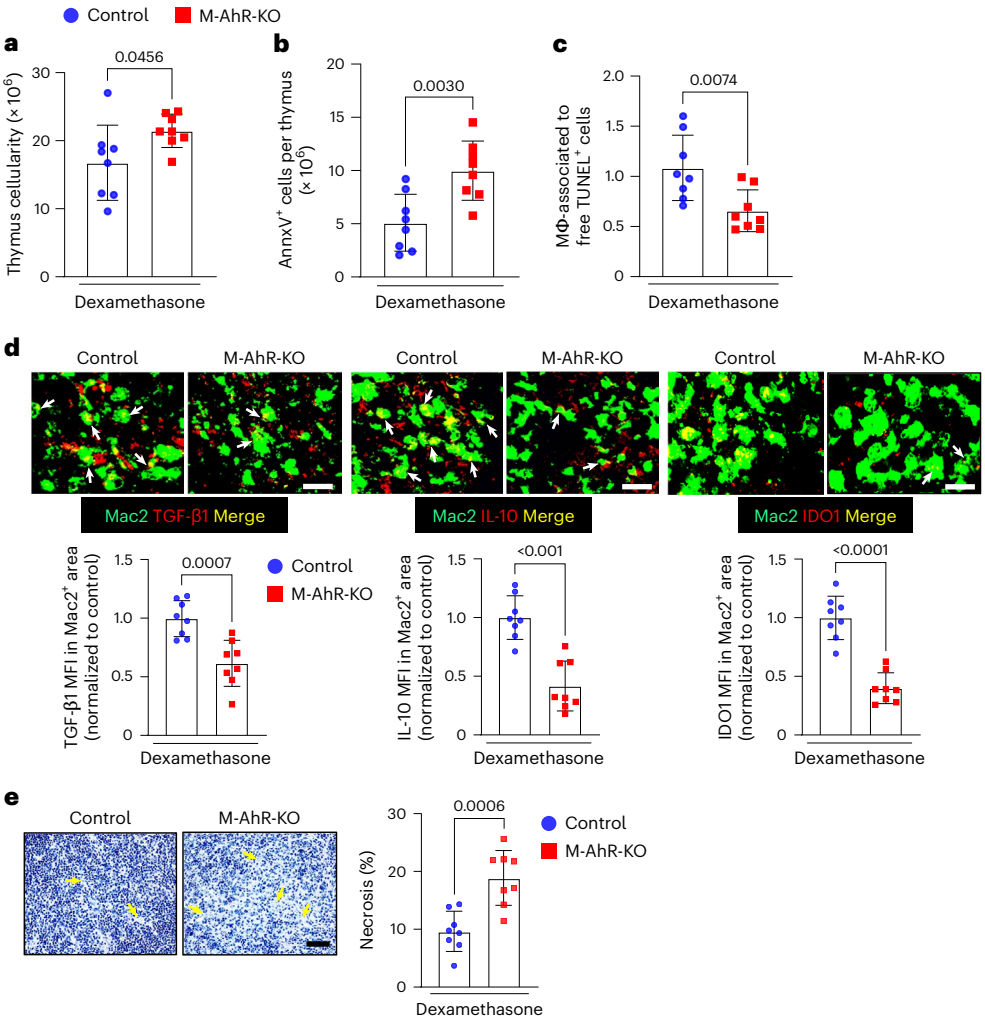

Fig. 7 | Macrophage AhR promotes efferocytosis and resolution in vivo. **a**–**e**, Mice were transplanted with BM from *Lyz2cre*$^{+/-}$ (control) or *Ahr*$^{fl/fl}$*Lyz2cre*$^{+/-}$ (M-AhR-KO) mice, and 4 weeks later were injected with dexamethasone. After 18 h, the thymi were collected and analysed as follows ($n = 8$ mice per group). **a**,**b**, Thymus cellularity and annexin V$^+$ (apoptotic) cells were analysed flow cytometry. **c**, Quantification of the ratio of macrophage-associated to free TUNEL$^+$ cells (efferocytosis) from analysis of immunofluorescence microscopy images. **d**, Thymi were immunostained for TGF-β1, IL-10 or IDO1 (red) and Mac2 (green). Scale bar, 50 µm. Arrows, examples of colocalization of TGF-β1 and Mac2 (left), IL-10 and Mac2 (centre) and IDO1 and Mac2 (right). The graphs show the quantification of TGF-β1, IL-10 and IDO1 MFI in Mac2$^+$ areas. **e**, Thymic necrosis, with quantification. Scale bar, 200 µm. Arrows, examples of necrotic areas. The data are expressed as mean ± s.e.m., and significance was determined by two-tailed Student's *t*-test or one-way ANOVA with Fisher's LSD post hoc analysis.

groups (Extended Data Fig. 8l). Most notably, whereas the necrotic area and lesion area were decreased and fibrous-cap thickness was increased in control regressing versus baseline lesions, as expected, these changes did not occur in the MΦ-IDO1-iKO cohort (Fig. 8c). Total lesion area in regression was also increased in the MΦ-IDO1-iKO group (Extended Data Fig. 8m). Moreover, whereas levels of TGF-β1 and IL-10 were increased in regressing versus baseline lesions in the control mice, which is consistent with the role of resolution in regression[10,12,13,48], these changes were markedly diminished in the MΦ-IDO1-iKO groups (Fig. 8d and Extended Data Fig. 8n).

The ratio of macrophage-associated to free TUNEL$^+$ cells was decreased in the Mac-IDO1-iKO regressing lesions, indicating impaired efferocytosis. The decrease in efferocytosis in the Mac-IDO1-iKO group was not associated with a change in thymic macrophages (Extended Data Fig. 8o). Finally, given that deletion of IDO1 in efferocytosing macrophages in vitro lowers nuclear AhR levels (described above), we assayed nuclear AhR in control and Mac-IDO1-iKO regressing lesions and found that it was decreased in the lesional macrophages of the Mac-IDO1-iKO cohort (Fig. 8e). Thus, macrophage IDO1 is necessary for the lowering of necrosis and the increase in fibrous-cap thickness in atherosclerosis regression, and efferocytosing macrophages in regressing lesions show evidence of the SLC36A4-IDO1-AhR pro-resolving pathway.

Discussion

The roles of IDO1 and AhR in immunobiology have been a topic of great interest over the last two decades[15,33–35]. The new concept in this study relates to how efferocytosis in mouse and human macrophages triggers a complex, pro-resolving metabolic programme that involves phagolysosomal degradation of ACs, upregulation of both the phagolysosomal Trp transporter SLC36A4 and IDO1, increased levels of the Trp metabolite Kyn and Kyn-dependent AhR activation. AhR activation separately triggers two key resolution pathways: (1) induction of *Il10*, *Tgfb1* and *Ido1* mRNA expression through a two-hit model requiring both Kyn and ERK1/2-mediated upregulation of AhR chaperones; and (2) continuing efferocytosis through the activation of Rac1. Increased *Ido1* mRNA expression and continuing efferocytosis likely contribute to a positive-feedback cycle. We provide evidence that this pathway promotes resolution and enhances efferocytosis in vivo, including in the key human-relevant process of atherosclerosis regression.

A previous study by Shinde et al.[49] investigating autoimmune disease reported that exposure of macrophages to ACs resulted in DNA-dependent activation of both toll-like receptor 9 (TLR9) and AhR, leading to suppression of inflammation. At the examined time point, the addition of ACs did not increase *Ido1* mRNA levels in the macrophages or the Kyn to Trp ratio in the cell culture medium, although data on cellular Trp metabolites were not reported[49]. Another study has shown that ACs upregulate a key enzyme in pro-resolving lipid mediator synthesis, ALOX12, which was blocked by inhibitors of TLR9 and AhR[50]. Data on IDO1 and Trp metabolite levels were not reported in the study. The link between TLR9 activation and IDO1- and Kyn-independent AhR activation was not identified in either work. Interestingly, previous work by the first group showed that TLR9 activation upregulates IDO1 in dendritic cells[51], but this mechanism is not consistent with the negative IDO1 data in Shinde et al.[49]. Another previous study by the same group reported that drug-induced inhibition of IDO promoted inflammation in mice injected with ACs[52]. However, rather than a role for Trp metabolism, the authors suggested a mechanism in which depletion of Trp by IDO1 quells inflammation by activating GCN2, a stress kinase that responds to amino acid deprivation[53]. This pathway was demonstrated in cells that were genetically manipulated to over express IDO1. Indeed, efferocytosis would be expected to supply Trp from AC engulfment and degradation, as shown here, not to deplete Trp. In contrast to these studies, we show that efferocytosis increases levels of SLC36A4, IDO1 and intracellular Trp and Trp metabolites, and we elucidate a detailed mechanism of how these processes, through AhR activation, promote post-efferocytic resolution in vitro and in vivo. For the in vivo studies, we used several models, including atherosclerosis regression, and showed not only a causative link to tissue resolution, but also a biochemical signature consistent with our pathway. Nonetheless, further studies are needed to understand the roles of different pathways that activate AhR and/or involve IDO1 in efferocytosing macrophages, which could involve issues related to timing, tissue environment and/or disease setting.

A key new finding in our study is that efferocytosis dramatically upregulates expression of the Trp transporter SLC36A4. SLC36A4, also known as PAT4, is an amino acid transporter with a high affinity for Trp[16] that has been shown to regulate the amino acid pool in the lysosomes of retinal pigment epithelial cells[17]. However, the role of SLC36A4 in efferocytosis was previously unknown. Our SLC36A4 causation data and the localization of the transporter in the vicinity of AC-containing phagolysosomes, when considered with previous knowledge about the roles of SLC36A4, support the hypothesis that SLC36A4 facilitates the transport of AC Trp from phagolysosomes into macrophages to provide substrate for the IDO1–Kyn–AhR resolution pathway described here. On the basis of prior work in $CD8^+$ T cells[54], it is also possible that SLC36A4 facilitates Kyn transport; this process could play a part if ACs have a substantial pool of Kyn, but our bafilomycin data suggest that protein hydrolysis has a major role as a source of Trp to feed the pathway. Our data also show that macrophages can use exogenous Trp to initiate the Kyn–AhR pathway under the following conditions: ERK1/2 is activated by ACs or PS beads; there is no ingested source of Trp (PS beads) or AC Trp is not available (si*Slc36a4*-transfected efferocytosing macrophages); and the medium is spiked with excess Trp, for example, 50 µM in our experiments. Finally, regarding the mechanism of efferocytosis-induced upregulation of SLC36A4, our work thus far suggests that a process downstream of AC internalization blocks the proteasomal degradation of SLC36A4, but how this occurs will require further study. A previous study has shown that the calcium transporter Orai1 associates with the E3 ligase cereblon (Crbn) in LR73 hamster fibroblasts, leading to Orai1's ubiquitination and proteasomal degradation, and that efferocytosis decreases Orai1–Crbn interaction by promoting the interaction of Orai1 with a competing protein, Stim1. This efferocytosis-mediated process decreased ubiquitination and proteasomal degradation of Orai1 and thereby increased Orai1 protein[21]. Whether a similar overall mechanism occurs with efferocytosis-induced stabilization of SLC36A4 remains to be examined.

Another key finding of our study is that AhR activation by efferocytosis-induced Kyn requires the activation of ERK1/2, which upregulates the AhR-stabilizing chaperones HSP90 and XAP2 (ref. 44,45). This pathway presumably enables Kyn to activate AhR–ARNT-mediated transcription, leading to increased expression of *Tgfb1*, *Il10* and *Ido1* mRNA. Of interest, a previous study has shown that MAP kinases promoted an increase in the transcriptional activity of ARNT, but not AhR, in a liver cancer cell line treated with environmental toxins, but a detailed mechanism was not reported[55]. Whether AhR and ARNT directly induce expression of the genes encoding *Tgfb1*, *Il10* and/or *Ido1* or lead to these increases through a secondary process, for example, by first increasing another transcription factor, remains to be elucidated. Future studies will also need to elucidate how the Kyn–AhR pathway activates Rac1, a key step in continuing efferocytosis, as well as how IDO1 facilitates primary efferocytosis, which is independent of AhR. In this context, the effect of myeloid IDO1-KO and myeloid AhR-KO were very similar in the dexamethasone–thymus model, suggesting that the effect of IDO1-KO on primary efferocytosis did not drive the phenotype, which is line with the importance of continuing efferocytosis in vivo[10,12,13].

We demonstrated the presence and functionality of the IDO1 pathway in vivo using both the dexamethasone–thymus model and, most importantly, atherosclerosis regression. Atherosclerosis regression is a human-relevant process triggered by marked lowering of LDL, and it is associated with features of plaque stabilization in mice and humans and with decreased risk for acute atherosclerotic coronary artery disease in humans[46,47]. The beneficial changes in plaque morphology in atherosclerosis regression, particularly the increase in fibrous-cap thickness, are driven in part by a reawakening of the macrophage efferocytosis–resolution cycle that becomes dormant in progressing atherosclerosis[10,12,48]. Our work indicates that macrophage IDO1 is necessary for the full regression response, and analyses of the lesions for the biochemical signature of the IDO1-AhR-resolution pathway are consistent with our

Fig. 8 | Macrophage IDO1 contributes to efferocytosis and features of plaque stabilization in atherosclerosis regression. a–**d**, *Ldlr*$^{-/-}$ mice were transplanted with BM from either *Ido1*$^{fl/fl}$ mice (control) or *Ido1*$^{fl/fl}$*Cx3cr1cre*$^{ERT2+/-}$ mice (inducible KO of IDO1 in macrophages, Mϕ-IDO1-iKO). After 4 weeks, the mice were fed a WD for 16 weeks, and cells from some of the mice were collected at this time (baseline). The remaining mice were then switched to a chow diet and injected with HDAd-LDLR virus to induce regression, and at the same time were given tamoxifen, which deletes IDO1 in macrophages in the Mϕ-IDO1-iKO cohort. After 7 weeks, the mice (the regression group) were killed and the aortic roots were harvested and analysed as follows. **a**,**b**, Regressing lesions from control mice were immunostained for IDO1 and SLC36A4, which were pseudocolored white, and efferocytosing macrophages were identified by colocalization of TUNEL stain (red) with Mac2 (macrophages; green). The MFI for IDO1 and SLC36A4 in efferocytosing ($TUNEL^+$) and non-efferocytosing ($TUNEL^-$) macrophages was quantified ($n = 10$ mice per group). Scale bar, 50 µm. Arrows, examples of colocalization of IDO1 or SLC36A4 with efferocytosing $TUNEL^+$ macrophages. **c**, H&E (top) and Sirius red staining (bottom) ($n = 9$–10 mice per group). Scale bar, 200 µm. The necrotic areas in the hematoxylin and eosin (H&E)-stained sections are outlined, with quantification shown in the graph. The Sirius-red-stained sections were used to measure fibrous-cap thickness at the lesional midpoint and both shoulder regions (block lines), which were then averaged for quantification. **d**, Quantification of TGF-β1 and IL-10 MFI, based on immunostaining, in $Mac2^+$ areas ($n = 9$–10 mice per group). **e**, The regressing lesions were immunostained for AhR (red), $Mac2^+$ macrophages (green) and $DAPI^+$ nuclei (blue). Arrows, AhR, DAPI and Mac2 colocalization. The graphs show the quantification of AhR nuclei in $Mac2^+$ areas ($n = 10$ mice per group). Scale bar, 50 µm. The data are expressed as mean ± s.e.m., and significance was determined by one-way ANOVA with Fisher's LSD post hoc analysis for **a** and **b** and by Student's *t*-test for **c** and **d**.

https://doi.org/10.1038/s42255-024-01115-7

in vitro mechanistic findings. To test our pathway in regression, we used a precise model in which IDO1 was inducibly deleted specifically in macrophages and only during regression. This model contrasts with a germline holo-IDO1-KO model used in two previous and contradictory atherosclerosis studies[56,57]. A study in *Ldlr*$^{-/-}$ mice that were fed a WD for 8 weeks concluded that IDO1 had a net pro-atherogenic effect, in contrast to our findings. The authors showed that germline holo-IDO1 KO in these mice reduced the lipid area of aortic root plaques and increased *Il10* mRNA levels in the spleen, which, on the basis of in vitro work with lipopolysaccharide-treated macrophages, was attributed

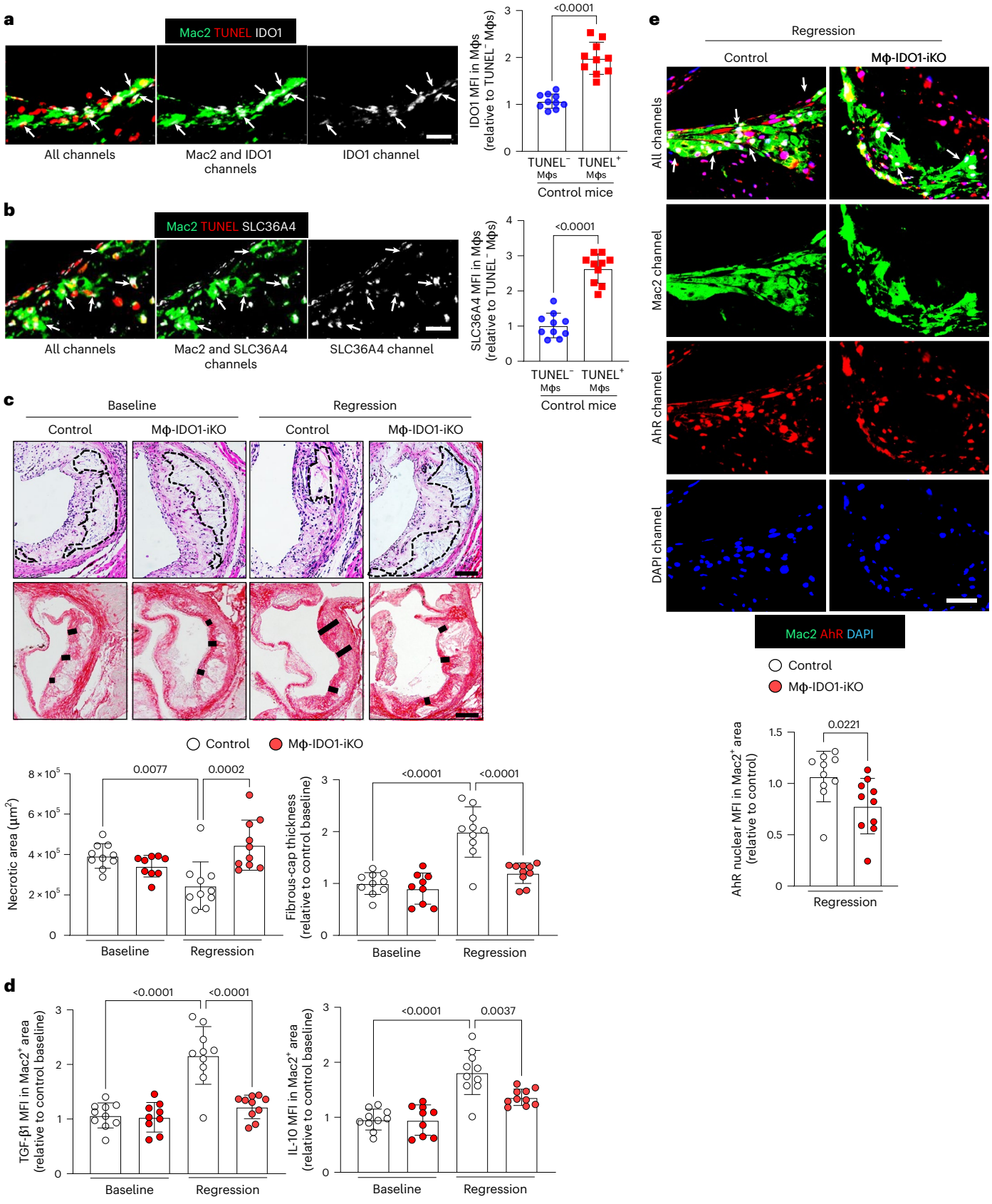

to abrogation by IDO1 KO of a kynurenic-acid-mediated pathway that normally lowers *Il10* levels[56]. This pathway in inflammatory macrophages is very different from the IDO1–Kyn–AhR pathway reported here that induces *Il10* in efferocytosing macrophages. A second study found that germline holo-IDO1 KO in *Apoe*$^{-/-}$ mice increased aortic root lesion area and lowered splenic IL-10 (ref. 57), which is consistent with the athero-protective role of IDO1 here. However, in this study, the athero-protective mechanism of IDO1 was suggested to be linked to the induction of IL-10 in B cells by anthranilic acid. To reiterate, the setting and models used for these two studies, that is, atherosclerosis progression and germline holo-knockout, are very different from the inducible macrophage-specific IDO1-KO regression model used here.

In progressing atherosclerosis, efferocytosis is impaired but not absent. Thus, a key issue regarding the potential translational implications of this study is whether the pro-resolving AhR pathway described here is dysfunctional in macrophages in progressing lesions and, if so, whether this impairment can be therapeutically reversed. Another question for future study is whether other AhR-activating Trp metabolites, for example, kynurenic acid, are involved, which could have relevance to human atherosclerosis[58]. Moreover, 3,3′-diindolylmethane, an AhR agonist with low toxicity that is present in certain vegetables, activates the Arg1–ornithine–Dbl pathway in macrophages[59], and AhR-induced CYP1A1 has been linked to Arg1 upregulation in macrophages[60]. We have previously shown that the efferocytosis-induced Arg1–ornithine–Dbl pathway promotes continuing efferocytosis in macrophages[10], and we now show that efferocytosis-induced *Arg1* and Dbl (*Mcf2*) require IDO1, suggesting that AhR activation contributes to this pathway in efferocytosing macrophages. However, AhR activation by certain ligands, notably environmental toxins, can promote pro-atherogenic inflammatory processes[61,62], suggesting that the athero-protective effects of AhR shown here could be ligand- or context-dependent, with efferocytosis setting the stage for a pro-resolving function of AhR. Related to this point, an exciting concept for the treatment of inflammatory diseases, including atherosclerosis, is efferocytosis-enhancing therapy, for example, through strategies that enhance endogenous macrophage efferocytosis or that use genetically engineered designer macrophages that excel at efferocytosis[63–66]. We imagine that these types of therapies, in combination with lowering LDL levels, could create an environment in which AhR activation is athero-protective by the mechanisms described herein. Finally, Kyn is a secretory molecule that we showed can rescue macrophages with deletion of IDO1 and SLC36A4, as long as there are signals to activate ERK1/2. Kyn production can be stimulated in macrophages in vitro by a type of anti-inflammatory cell therapy that promotes efferocytosis[67]. Thus, it is possible that Kyn secreted by a limited number of therapeutically improved efferocytic macrophages could jump-start the efferocytosis–resolution cycle in lesional macrophages and thereby prevent further plaque progression and promote processes involved in plaque stabilization. It is also possible that Trp supplementation could achieve the same goal, and several studies have shown that high concentrations of Trp in plasma are associated with a decreased risk of cardiovascular disease[68–70]. In this context, an important challenge in pro-efferocytosis and resolution therapy in general[71], and for therapies that boost macrophage Trp metabolism in particular[72], is to avoid activating an immunosuppressive response that could lower defence against tumour cells.

Methods

Experimental animals

Mouse protocols were approved by Columbia University's Institutional Animal Care and Use Committee, and the mice were cared for according to National Institutes of Health (NIH) guidelines for the care and use of laboratory animals. The mice were housed in standard cages at room temperature, 30–70% humidity, with a 12-h light and 12-h dark cycle in a barrier facility with ad libitum access to water and food. Male C57BL/6J wild-type mice (8–10 weeks old) that were purchased from The Jackson Laboratory (strain no. 000664) were used as bone-marrow transplant (BMT)-recipient mice for the zymosan A1 and dexamethasone–thymus experiments; the numbers of mice used in each experiment are indicated in the figure legends. Male *Ldlr*$^{-/-}$ mice (8 10 weeks old) mice on the C57BL/6J background (B6.129S7-Ldlr^{tm1Her}/J; Jackson Laboratory, strain no. 002207) were used as BMT-recipient mice for the atherosclerosis experiments. All purchased mice were allowed to adapt to housing in the animal facility for 1 week before the experiments began. For BMT donor mice, we used 8- to 10-week-old *Lyz2cre*$^{+/-}$ (control) and *Ido1*$^{fl/fl}$*Lyz2cre*$^{+/-}$ (M-IDO1-KO) male mice, both on the C57BL/6J background, as described[73]. *Lyz2cre*$^{+/-}$ mice were purchased from The Jackson Laboratory (strain no. 004781). *Ahr*$^{fl/fl}$ mice were purchased from The Jackson Laboratory (strain no. 006203). *Ido1*$^{fl/fl}$*Cx3cr1cre*^{ERT2} mice were bred using *Cx3cr1cre*^{ERT2} mice purchased from The Jackson Laboratory (strain no. 020940). The ratio of donor to recipient mice for BMT was 10:1. Investigators were blinded for atherosclerosis experiments but were not blinded for zymosan-induced peritonitis and dexamethasone–thymus experiments.

Generation of BMDMs

Bone-marrow cells from either male or female 8- to 10-week-old mice were cultured in DMEM (Thermo Fisher Scientific) supplemented with 10% heat-inactivated FBS, 100 mg ml^{-1} streptomycin and 10 U ml^{-1} penicillin (all from Thermo Fisher Scientific) and with 20% L-929 fibroblast-conditioned medium. After 6–8 d, these BMDMs were used for the indicated experiments.

Generation of HMDMs

White blood cells were isolated from the buffy coats of de-identified healthy adult donors, who provided their consent (sourced from the New York Blood Center). Monocytes were purified in a discontinuous gradient of Histopaque solution and then placed in 24-well culture plates in a humidified CO_2 incubator maintained at 37 °C. After 4 h to allow for adhesion, the monolayers were rinsed to remove non-adherent cells. The culture medium was then replaced with RPMI-1640 (Thermo Fisher Scientific) containing 10% heat-inactivated FBS, 100 mg ml^{-1} streptomycin, 10 U ml^{-1} penicillin and 20 ng ml^{-1} GM-CSF (Peprotech). After 10 d, the HMDMs were used for experiments.

Cell lines

Jurkat human T lymphocytes (TIB-152) and L-929 mouse fibroblasts (CCL-1) were obtained from the American Type Culture Collection and cultured in DMEM supplemented with 10% (vol/vol) heat-inactivated FBS, 10 U ml^{-1} penicillin and 100 mg ml^{-1} streptomycin. The cells were cultured in a humidified CO_2 incubator at 37 °C.

Induction of apoptosis and labelling of apoptotic cells

Jurkat cells were irradiated for 15 min under an ultraviolet (UV) amp with a wavelength of 254 nm, followed by incubation in PBS for 2–3 h before use for experiments. For some experiments, the ACs were rinsed once with serum-free DMEM and then suspended in Vybrant DiD cell-labelling solution (Invitrogen) at a concentration of 2×10^7 cells ml^{-1} for 10 min, or they were suspended 1 ml of Diluent C (Sigma-Aldrich) containing PKH26 or PKH67 dye (Sigma-Aldrich) for 5 min. The labelling reactions were neutralized with 2 ml of FBS. The ACs were then rinsed twice with DMEM containing 10% heat-inactivated FBS and used for experiments. For other experiments, ACs were stained with pHrodo dye (Thermo Fisher Scientific), per the manufacturer's protocol. For experiments using apoptotic macrophages, HMDMs were treated with 1 µM staurosporine in DMEM medium for 48 h and then incubated with BMDMs.

In vitro efferocytosis assay

BMDMs were seeded in 24-well plates at a density of 0.18×10^6 cells per well. The macrophages were then incubated with PKH26-labelled ACs

for 45 min at a 10:1 AC:macrophage ratio, followed by three washes with PBS (primary efferocytosis) and then incubation for an additional 2 h in normal cell culture medium, followed by the addition of PKH67-labelled ACs for 45 min (continuing efferocytosis). At the end of the incubation periods, the macrophages were washed three times with PBS to remove unattached ACs, followed by fixation with 4% PFA for 20 min and, after rinsing three times with PBS, visualization under a Leica DMI6000B epifluorescence microscope.

Polystyrene beads

Ten-micrometre streptavidin-coated polystyrene beads (Thermo Fisher Scientific) were used as-is or conjugated to PS by incubation with biotinylated PS, as previously described[74]. The beads were then incubated with macrophages.

Immunoblotting

Cells or nuclear extracts, which were prepared using the Cell Fractionation Kit from Cell Signal\ling, according to the manufacturer's instructions, were lysed in 2× Laemmli lysis buffer (Bio-Rad) containing 50 mM dithiothreitol. Lysates were heated at 95 °C for 5 min, separated on 4%–20% SDS–PAGE gradient gels (Invitrogen) at 120 V for 120 min and electrotransferred to 0.45-mm-thick polyvinylidene difluoride membranes at 100 V for 90–120 min. The membranes were incubated overnight at 4 °C with primary antibodies in TBST (Tris-buffered saline + Tween 20) containing 5% BSA and then with horseradish-peroxidase-conjugated secondary antibodies (Pierce). The antibodies are listed in Supplementary Table 4. Densitometric evaluations were performed using 2.0 myImageAnalysis software (Thermo Fisher Scientific).

Immunoprecipitation

IP lysis buffer supplemented with a protease and phosphatase inhibitor cocktail (Thermo Fisher Scientific) was used to lyse BMDMs. The lysates were homogenized through a 25-gauge needle five times and incubated for 15 min on ice. Lysates were then centrifuged at 16,000*g* for 10 min at 4 °C, and the supernatant fractions were transferred to new tubes and incubated with control rabbit IgG (CST Technology Solutions, CST no. 3900; 1:250) or anti-ARNT (CST no. 5537; 1:50) overnight at 4 °C with rotation. Next, 30 µl of Protein A magnetic beads (CST no. 73778) was added to each of the samples, which were incubated for 2–3 h at 4 °C with rotation. The beads were rinsed five times with IP lysis buffer (without protease and phosphatase inhibitors) and resuspended in 50 µl 2× Laemmli sample buffer, and the solution was then boiled for 5 min at 95 °C and used for immunoblot analysis. The antibodies are listed in Supplementary Table 4.

ELISA

TGF-β1 and IL-10 were measured in the peritoneal exudates using commercial ELISA kits purchased from Biolegend and Cayman Chemicals, respectively, and the assays were conducted as per the manufacturer's protocol.

siRNA-mediated gene silencing

siRNA (50 nM) or scrambled control RNA (Supplementary Table 5) was transfected into macrophages using Lipofectamine RNAiMAX (Life Technologies), following the manufacturer's protocol. In brief, cells seeded in 450 µl of BMDM medium were incubated with 50 µl of OptiMEM containing 1.5 µl iMAX and 50 nM siRNA. The experiments were conducted after 48 h or 72 h. To validate silencing efficiency, gene expression or immunoblot analyses were performed.

Quantitative real-time PCR

RNA was isolated from samples using the PureLink RNA Mini Kit (Life Technologies), adhering to the manufacturer's guidelines. To ascertain the purity and concentration of the RNA, NanoDrop spectrophotometry (Thermo Fisher Scientific) was used. Complementary DNA was synthesized from 200 ng of RNA from the samples (260/280 ratio > 1.8) utilizing oligo (dT) and Superscript II (Applied Biosystems). Quantitative real-time PCR was performed using a 7500 Real-Time PCR system (Applied Biosystems) and SYBR Green Master Mix reagents (Applied Biosystems). All sequences for primers are listed in Supplementary Table 5.

Flow cytometry

After fixation in 4% PFA (Thermo Fisher Scientific), cells were resuspended in FACS staining buffer (BioLegend)) and incubated with mouse TruStain FcX PLUS (CD16/32, Biolegend) Fc-blocking antibody (Biolegend). Cell-surface receptor staining was carried out by incubating the cells with fluorescent antibodies for 1 h at 4 °C. Cells were permeabilized with BD Perm/Wash (BD Biosciences) for intracellular staining, followed by incubation with fluorescent antibodies for 1 h at 4 °C. The antibodies are listed in Supplementary Table 4. The cells were then washed in FACS buffer (twice) and resuspended for analysis on a BD FACS Canto II flow cytometer. For apoptosis detection, cells were washed with cold FACS buffer (twice), resuspended in annexin-V-binding buffer at a concentration of 1×10^6 cells ml^{-1}, and incubated with fluorescein isothiocyanate (FITC)-conjugated antibody to annexin V for 15–20 min at room temperature. The samples were then analysed by a BD FACS Canto II flow cytometer. Data analysis was done using FlowJo v.10.

Zymosan-induced peritonitis and uptake of apoptotic neutrophils

To induce sterile peritonitis, male mice (8–10 weeks old) were injected i.p. with 1 ml of 1 mg ml^{-1} zymosan A (Sigma-Aldrich). Peritoneal exudates were collected and assayed for TGF-β1 and IL-10 using ELISA. To quantify neutrophil numbers, cells in the exudate were stained with mouse anti-Ly6G (Biolegend) and assayed by flow cytometry. To assess the macrophage uptake of neutrophils, exudate cells were stained with anti-F4/80 antibody (Biolegend) to identify macrophages and then permeabilized and stained with anti-Ly6G to assay neutrophils that had been internalized by macrophages, that is, F4/80$^+$Ly6G$^+$ macrophages.

Dexamethasone–thymus experiment

Mice were injected i.p. with 250 µl of PBS containing 250 mg of dexamethasone (Sigma-Aldrich) dissolved in dimethyl sulfoxide. After 18 h, the mice were euthanized, and the thymi were collected and weighed. Next, one lobe of the thymus was mechanically disaggregated, and cell count was determined using Countess II (Invitrogen). Cells (1×10^6) were then stained with either FITC-conjugated annexin V antibody (Biolegend) for apoptotic cell detection or anti-F4/80 antibody (Biolegend) for macrophage number. The other lobe was fixed in 4% PFA, sectioned and immunostained with TUNEL reagent (Roche), anti-TGFβ1 (Abcam), anti-IL-10 (Cell Signaling), anti-IDO1 (Cell Signaling), and/or anti-Mac2 antibodies (Cedarlane). Efferocytosis was measured by counting TUNEL$^+$ cells that were associated with Mac2$^+$ cells, that is, TUNEL$^+$ nuclei in the cytoplasm of, or in contact with, Mac2$^+$ macrophages, versus macrophage-free TUNEL$^+$ cells, that is, TUNEL$^+$ nuclei not in contact with neighbouring macrophages. To test the effect of Kyn, mice were injected i.p. with 100 mg kg^{-1} Kyn 1 h before and after dexamethasone injection, followed by Kyn supplementation (5 mM) in the drinking water until the mice were euthanized.

Atherosclerosis experiment

Ldlr$^{-/-}$ mice (8–10 weeks old) were irradiated with 1,000 rads using a caesium-137 GammaCell source. On the same day, the mice were injected intravenously with 2.5×10^6 BM cells from littermate control *Ido1*$^{fl/fl}$ mice or *Ido1*$^{fl/fl}$*Cx3cr1cre*$^{CreERT2/+}$ (Mϕ-IDO1-iKO) mice and then given acidic water containing 10 mg ml^{-1} neomycin. Starting 4 weeks later, the mice were fed a WD (Envigo, TD 88137) for 16 weeks.

Aortic roots from one cohort ('baseline') were harvested at this time, while the other cohort ('regression') was injected intravenously with a helper-dependent adenovirus containing the human LDLR gene (HDAd-LDLR) and then placed on a chow diet for an additional 7 weeks, as previously described[10,12]. The following work-up of the mice and all atherosclerosis measurements were conducted as previously described[10,12,13]. In brief, the mice were fasted overnight, and blood glucose was assayed the next morning using a OneTouch Ultra device. Plasma total cholesterol was measured using a Wako Diagnostics kit, according to the manufacturer's instructions, and complete blood cell counts and the leucocyte differential count were measured using a FORCYTE Hematology Analyzer (Oxford Science). Following euthanasia of the mice, PBS was perfused through the left ventricle. Aortic roots were histologically processed and stained with H&E. For each mouse, six sections that were 30 µm apart were quantified, starting at the aortic root base. The area from the internal elastic lamina to the lumen (total lesion area) was quantified using image analysis software. The aortic lesions were also stained for necrotic areas and collagen using picrosirius red (Polysciences, catalogue no. 24901A), as previously described[10,12,13].

Tissue immunohistochemistry and immunofluorescence microscopy

Paraffin-embedded 6-µm sections were deparaffinized with xylene and rehydrated using an ethanol gradient. Sections were incubated with TUNEL staining reagent at 37 °C for 1 h and then washed with PBS (three times). Alternatively, rehydrated sections were blocked with 2% BSA in PBS for 1 h and then immunostained with anti-Mac2, anti-AhR, anti-TGF-β1 or anti-IL10 antibodies overnight at 4 °C. The sections were incubated with fluorescently labelled secondary antibodies and counterstained with 4,6-diamidino-2-phenylindole (DAPI). Images were visualized under a Leica DMI6000B epifluorescence microscope.

Confocal microscopy imaging

PKH26-labelled ACs were added at a 10:1 ratio of ACs to macrophages for 45 min, after which the macrophages were rinsed with PBS and then fixed with 4% PFA for 15 min at room temperature. Images were acquired using a NIKON A1 confocal microscope and analysed using ImageJ software.

Profiling of Trp metabolites using ultra-high-pressure LC–MS

Macrophage monolayers were placed on ice and, after removal of the medium, rinsed with ice-cold 150 mM ammonium acetate in Milli-Q water (HPLC grade). The cells were then extracted in 0.8 ml per well of ice-cold methanol for 15 min and scraped into tubes, and each well was then washed with 0.6 ml of Milli-Q water, which was added to the tubes (total volume per tube, 1.4 ml). The solvent was then dried under a stream of nitrogen at room temperature and dissolved in LC loading solvent (water containing 0.1% formic acid) spiked with 50 ng of [D_4]Kyn and [$^{13}C_{11}$-]Trp for LC–MS analysis. For metabolite profiling, a reference protocol[75] was optimized for an assay targeting L-Trp and several metabolites, including DL-Kyn, *N*-formylkynurenine, kynurenic acid, quinolinic acid, anthranilic acid, 3-hydroxyanthranilic acid, 2-picolinic acid, xanthurenic acid, nicotinic acid, nicotinamide, nicotinamide adenine dinucleotide$^+$, serotonin, melatonin, indole and tryptamine, using ultra-high-performance liquid chromatography coupled to high-resolution mass spectrometry (UHPLC-HRMS) on a Vanquish and Q Exactive Focus (Thermo Fisher Scientific). Separation was performed on a reversed-phase Waters Atlantis T3 column (2.1 mm inner diameter ×150 mm length with 3-µm particle size). The column was maintained at 25 °C with a 0.400 ml min^{-1} flow rate. Solvent A was composed of HPLC grade water containing 0.1% formic acid (FA); Solvent B was acetonitrile containing 0.1% FA. A linear gradient was programmed from 0 to 40% B (100% to 60% A) over 10 min, then from 40% to 95% B over 2 min, followed by 95% to 0% B over 0.1 min, then re-equilibrated for 5 min at 0% B for a total run time of 17 min. The Q Exactive Focus mass spectrometer was equipped with a heated electrospray ionization (HESI) probe and operated in positive ion mode using Full MS for quantification. The analytes were detected using Full Scan with the following parameters: spray voltage 3.5 kV, 70,000 resolution, 100 ms maximum injection time and scan range from 100 to 680 *m/z*. Neat tryptophan metabolite standards as well as the stable isotope standards, [D_4]Kyn and [$^{13}C_{11}$]Trp, were prepared in 80% methanol at a concentration of 1 mg ml^{-1} and diluted with LC loading solvent to 1 µg ml^{-1}. The stable isotope standards were further diluted to 50 ng µl^{-1}. Peak heights for the Trp and its metabolites, as well as the respective stable isotope standards, were extracted from the chromatograms using XCalibur Quan Browser (version 4.2.47, Thermo Fisher Scientific) and normalized to the amount of protein in the sample.

Rac1 activity assay

BMDMs were plated on 12-well plates and incubated with 10-µm polystyrene beads at a macrophage:bead ratio of 1:10. The cells were then washed and lysed with RIPA buffer containing Halt Protease and Phosphatase Inhibitor Cocktail (Thermo Fisher Scientific). Precision Red Advanced Protein Assay (Cytoskeleton) was used to determine protein concentrations. Rac1 activity was measured using the Rac1 G-LISA Activation Assay Kit (Cytoskeleton), per the manufacturer's instructions.

Statistical analyses

The Shapiro–Wilk test was used for testing normality, and GraphPad Prism software (v. 10.2.3) was used to determine statistical significance. All the data in this study fit a normal distribution, and *P* values were determined using either the Student's *t*-test for two groups or one-way ANOVA with Fisher's LSD post hoc analysis when three or more groups were tested. Data are shown as mean values ± s.e.m. Differences were considered statistically significant at $P < 0.05$. On the basis of our prior research on mouse atherosclerosis and power calculations, the number of mice chosen for each cohort was sufficient to ensure the testing of our hypotheses, on the basis of an expected 20%–30% coefficient of variations and an 80% probability of identifying a 33% difference in crucial plaque metrics, for example fibrous-cap thickness and necrotic area. Initial exclusion criteria for the in vivo studies included death, injury requiring euthanasia or weight loss of >15% body weight, but only one mouse was excluded in this study, which was for injury in the atherosclerosis experiment. For the cell culture studies, no statistical methods were used to predetermine sample sizes, but our sample sizes are like those reported in previous publications[10,12,13,76,77]. For all experiments, *n* represents the number of independent replicates.

Reporting summary

Further information on research design is available in the Nature Portfolio Reporting Summary linked to this article.

Data availability

All data supporting the study are available in the manuscript and supplementary information. Source data are provided with this paper.

References

1. Panigrahy, D., Gilligan, M. M., Serhan, C. N. & Kashfi, K. Resolution of inflammation: an organizing principle in biology and medicine. *Pharmacol. Ther.* **227**, 107879 (2021).
2. Nathan, C. & Ding, A. Nonresolving inflammation. *Cell* **140**, 871–882 (2010).
3. Hochreiter-Hufford, A. & Ravichandran, K. S. Clearing the dead: apoptotic cell sensing, recognition, engulfment, and digestion. *Cold Spring Harb. Perspect. Biol.* **5**, a008748 (2013).
4. Morioka, S., Maueroder, C. & Ravichandran, K. S. Living on the edge: efferocytosis at the interface of homeostasis and pathology. *Immunity* **50**, 1149–1162 (2019).

5. Doran, A. C., Yurdagul, A. Jr. & Tabas, I. Efferocytosis in health and disease. *Nat. Rev. Immunol.* **20**, 254–267 (2020).
6. Henson, P. M. Cell removal: efferocytosis. *Annu. Rev. Cell Dev. Biol.* **33**, 127–144 (2017).
7. Linton, M. F. et al. Macrophage apoptosis and efferocytosis in the pathogenesis of atherosclerosis. *Circ. J.* **80**, 2259–2268 (2016).
8. Kojima, Y., Weissman, I. L. & Leeper, N. J. The role of efferocytosis in atherosclerosis. *Circulation* **135**, 476–489 (2017).
9. A-Gonzalez, N. et al. Apoptotic cells promote their own clearance and immune tolerance through activation of the nuclear receptor LXR. *Immunity* **31**, 245–258 (2009).
10. Yurdagul, A. Jr. et al. Macrophage metabolism of apoptotic cell-derived arginine promotes continual efferocytosis and resolution of injury. *Cell Metab.* **31**, 518–533 (2020).
11. Yurdagul, A. Jr. et al. ODC (ornithine decarboxylase)-dependent putrescine synthesis maintains MerTK (MER tyrosine-protein kinase) expression to drive resolution. *Arterioscler. Thromb. Vasc. Biol.* **41**, e144–e159 (2021).
12. Gerlach, B. D. et al. Efferocytosis induces macrophage proliferation to help resolve tissue injury. *Cell Metab.* **33**, 2445–2463 (2021).
13. Ampomah, P. B. et al. Macrophages use apoptotic cell-derived methionine and DNMT3A during efferocytosis to promote tissue resolution. *Nat. Metab.* **4**, 444–457 (2022).
14. Zhang, S. et al. Efferocytosis fuels requirements of fatty acid oxidation and the electron transport chain to polarize macrophages for tissue repair. *Cell Metab.* **29**, 443–456 (2018).
15. Moffett, J. R. & Namboodiri, M. A. Tryptophan and the immune response. *Immunol. Cell Biol.* **81**, 247–265 (2003).
16. Pillai, S. M. & Meredith, D. SLC36A4 (hPAT4) is a high affinity amino acid transporter when expressed in *Xenopus laevis* oocytes. *J. Biol. Chem.* **286**, 2455–2460 (2011).
17. Shang, P. et al. The amino acid transporter SLC36A4 regulates the amino acid pool in retinal pigmented epithelial cells and mediates the mechanistic target of rapamycin, complex 1 signaling. *Aging Cell* **16**, 349–359 (2017).
18. Park, S. Y. et al. Rapid cell corpse clearance by stabilin-2, a membrane phosphatidylserine receptor. *Cell Death Differ.* **15**, 192–201 (2008).
19. Flannagan, R. S., Canton, J., Furuya, W., Glogauer, M. & Grinstein, S. The phosphatidylserine receptor TIM4 utilizes integrins as coreceptors to effect phagocytosis. *Mol. Biol. Cell* **25**, 1511–1522 (2014).
20. Williamson, A. P. & Vale, R. D. Spatial control of Draper receptor signaling initiates apoptotic cell engulfment. *J. Cell Biol.* **217**, 3977–3992 (2018).
21. Moon, H. et al. Crbn modulates calcium influx by regulating Orai1 during efferocytosis. *Nat. Commun.* **11**, 5489 (2020).
22. Pallotta, M. T. et al. Indoleamine 2,3-dioxygenase 1 (IDO1): an up-to-date overview of an eclectic immunoregulatory enzyme. *FEBS J.* **289**, 6099–6118 (2022).
23. Yoshimori, T., Yamamoto, A., Moriyama, Y., Futai, M. & Tashiro, Y. Bafilomycin A1, a specific inhibitor of vacuolar-type H^+-ATPase, inhibits acidification and protein degradation in lysosomes of cultured cells. *J. Biol. Chem.* **266**, 17707–17712 (1991).
24. Park, D. et al. Continued clearance of apoptotic cells critically depends on the phagocyte Ucp2 protein. *Nature* **477**, 220–224 (2011).
25. Koblish, H. K. et al. Hydroxyamidine inhibitors of indoleamine-2,3-dioxygenase potently suppress systemic tryptophan catabolism and the growth of IDO-expressing tumors. *Mol. Cancer Ther.* **9**, 489–498 (2010).
26. Liu, X. et al. Selective inhibition of IDO1 effectively regulates mediators of antitumor immunity. *Blood* **115**, 3520–3530 (2010).
27. Ravichandran, K. S. & Lorenz, U. Engulfment of apoptotic cells: signals for a good meal. *Nat. Rev. Immunol.* **7**, 964–974 (2007).
28. Proto, J. D. et al. Regulatory T cells promote macrophage efferocytosis during inflammation resolution. *Immunity* **49**, 666–677.e666 (2018).
29. Vallés, A. M., Beuvin, M. & Boyer, B. Activation of Rac1 by paxillin–Crk–DOCK180 signaling complex is antagonized by Rap1 in migrating NBT-II cells. *J. Biol. Chem.* **279**, 44490–44496 (2004).
30. Fadok, V. A. et al. Macrophages that have ingested apoptotic cells in vitro inhibit proinflammatory cytokine production through autocrine/paracrine mechanisms involving TGF-β, PGE2, and PAF. *J. Clin. Invest.* **101**, 890–898 (1998).
31. Cervenka, I., Agudelo, L. Z. & Ruas, J. L. Kynurenines: tryptophan's metabolites in exercise, inflammation, and mental health. *Science* **357**, eaaf9794 (2017).
32. Navarro-Xavier, R. A. et al. A new strategy for the identification of novel molecules with targeted proresolution of inflammation properties. *J. Immunol.* **184**, 1516–1525 (2010).
33. Hezaveh, K. et al. Tryptophan-derived microbial metabolites activate the aryl hydrocarbon receptor in tumor-associated macrophages to suppress anti-tumor immunity. *Immunity* **55**, 324–340 (2022).
34. Campesato, L. F. et al. Blockade of the AHR restricts a T_{reg}–macrophage suppressive axis induced by L-kynurenine. *Nat. Commun.* **11**, 4011 (2020).
35. Nguyen, N. T. et al. Aryl hydrocarbon receptor and kynurenine: recent advances in autoimmune disease research. *Front Immunol.* **5**, 551 (2014).
36. Mezrich, J. D. et al. An interaction between kynurenine and the aryl hydrocarbon receptor can generate regulatory T cells. *J. Immunol.* **185**, 3190–3198 (2010).
37. Opitz, C. A. et al. An endogenous tumour-promoting ligand of the human aryl hydrocarbon receptor. *Nature* **478**, 197–203 (2011).
38. Tsuji, N. et al. The activation mechanism of the aryl hydrocarbon receptor (AhR) by molecular chaperone HSP90. *FEBS Open Bio.* **4**, 796–803 (2014).
39. Kim, S. H. et al. Novel compound 2-methyl-2*H*-pyrazole-3-carboxylic acid (2-methyl-4-*o*-tolylazo-phenyl)-amide (CH-223191) prevents 2,3,7,8-TCDD-induced toxicity by antagonizing the aryl hydrocarbon receptor. *Mol. Pharmacol.* **69**, 1871–1878 (2006).
40. Vogel, C. F., Goth, S. R., Dong, B., Pessah, I. N. & Matsumura, F. Aryl hydrocarbon receptor signaling mediates expression of indoleamine 2,3-dioxygenase. *Biochem. Biophys. Res. Commun.* **375**, 331–335 (2008).
41. Hoffman, E. C. et al. Cloning of a factor required for activity of the Ah (dioxin) receptor. *Science* **252**, 954–958 (1991).
42. Park, S. Y. et al. Stabilin-1 mediates phosphatidylserine-dependent clearance of cell corpses in alternatively activated macrophages. *J. Cell Sci.* **122**, 3365–3373 (2009).
43. Favata, M. F. et al. Identification of a novel inhibitor of mitogen-activated protein kinase kinase. *J. Biol. Chem.* **273**, 18623–18632 (1998).
44. Cox, M. B. & Miller, C. A. III Cooperation of heat shock protein 90 and p23 in aryl hydrocarbon receptor signaling. *Cell Stress Chaperones* **9**, 4–20 (2004).
45. Pappas, B. et al. p23 protects the human aryl hydrocarbon receptor from degradation via a heat shock protein 90-independent mechanism. *Biochem. Pharmacol.* **152**, 34–44 (2018).
46. Raber, L. et al. Effect of alirocumab added to high-intensity statin therapy on coronary atherosclerosis in patients with acute myocardial infarction: the PACMAN-AMI Randomized Clinical Trial. *JAMA* **327**, 1771–1781 (2022).

47. Nicholls, S. J. et al. Effect of evolocumab on coronary plaque phenotype and burden in statin-treated patients following myocardial infarction. *JACC Cardiovasc. Imaging* **15**, 1308–1321 (2022).
48. Sharma, M. et al. Regulatory T cells license macrophage pro-resolving functions during atherosclerosis regression. *Circ. Res.* **127**, 335–353 (2020).
49. Shinde, R. et al. Apoptotic cell-induced AhR activity is required for immunological tolerance and suppression of systemic lupus erythematosus in mice and humans. *Nat. Immunol.* **19**, 571–582 (2018).
50. Koenis, D. S., de Matteis, R., Rajeeve, V., Cutillas, P. & Dalli, J. Efferocyte-derived MCTRs metabolically prime macrophages for continual efferocytosis via Rac1-mediated activation of glycolysis. *Adv. Sci.* **11**, e2304690 (2023).
51. Mellor, A. L. et al. Cutting edge: CpG oligonucleotides induce splenic CD19$^+$ dendritic cells to acquire potent indoleamine 2,3-dioxygenase-dependent T cell regulatory functions via IFN type 1 signaling. *J. Immunol.* **175**, 5601–5605 (2005).
52. Ravishankar, B. et al. Tolerance to apoptotic cells is regulated by indoleamine 2,3-dioxygenase. *Proc. Natl Acad. Sci. USA* **109**, 3909–3914 (2012).
53. Ravishankar, B. et al. The amino acid sensor GCN2 inhibits inflammatory responses to apoptotic cells promoting tolerance and suppressing systemic autoimmunity. *Proc. Natl Acad. Sci. USA* **112**, 10774–10779 (2015).
54. Liu, Y. et al. Tumor-repopulating cells induce PD-1 expression in CD8$^+$T cells by transferring kynurenine and AhR activation. *Cancer Cell* **33**, 480–494 (2018).
55. Tan, Z., Huang, M., Puga, A. & Xia, Y. A critical role for MAP kinases in the control of Ah receptor complex activity. *Toxicol. Sci.* **82**, 80–87 (2004).
56. Metghalchi, S. et al. Indoleamine 2,3-dioxygenase fine-tunes immune homeostasis in atherosclerosis and colitis through repression of interleukin-10 production. *Cell Metab.* **22**, 460–471 (2015).
57. Cole, J. E. et al. Indoleamine 2,3-dioxygenase-1 is protective in atherosclerosis and its metabolites provide new opportunities for drug development. *Proc. Natl Acad. Sci. USA* **112**, 13033–13038 (2015).
58. Baumgartner, R. et al. Evidence that a deviation in the kynurenine pathway aggravates atherosclerotic disease in humans. *J. Intern Med* **289**, 53–68 (2021).
59. Yang, L., Zheng, C., Xia, Y. F., Dai, Y. & Wei, Z. F. 3,3′-diindolylmethane enhances macrophage efferocytosis and subsequently relieves visceral pain via the AhR/Nrf2/Arg-1-mediated arginine metabolism pathway. *Phytomedicine* **116**, 154874 (2023).
60. Tian, L. X. et al. Cytochrome P450 1A1 enhances arginase-1 expression, which reduces LPS-induced mouse peritonitis by targeting JAK1/STAT6. *Cell Immunol.* **349**, 104047 (2020).
61. Zhu, K. et al. Aryl hydrocarbon receptor pathway: role, regulation and intervention in atherosclerosis therapy. *Mol. Med. Rep.* **20**, 4763–4773 (2019).
62. Wu, D. et al. Activation of aryl hydrocarbon receptor induces vascular inflammation and promotes atherosclerosis in apolipoprotein E$^{-/-}$ mice. *Arterioscler. Thromb. Vasc. Biol.* **31**, 1260–1267 (2011).
63. Mehrotra, P. & Ravichandran, K. S. Drugging the efferocytosis process: concepts and opportunities. *Nat. Rev. Drug Discov.* **21**, 601–620 (2022).
64. Morioka, S. et al. Chimeric efferocytic receptors improve apoptotic cell clearance and alleviate inflammation. *Cell* **185**, 4887–4903 (2022).
65. Kojima, Y. et al. CD47-blocking antibodies restore phagocytosis and prevent atherosclerosis. *Nature* **536**, 86–90 (2016).
66. Flores, A. M. et al. Pro-efferocytic nanoparticles are specifically taken up by lesional macrophages and prevent atherosclerosis. *Nat. Nanotechnol.* **15**, 154–161 (2020).
67. Schrodt, M. V. et al. Efferocytosis of viable versus heat-inactivated MSC induces human monocytes to distinct immunosuppressive phenotypes. *Stem Cell Res. Ther.* **14**, 206 (2023).
68. Li, Q. et al. Associations between plasma tryptophan and indole-3-propionic acid levels and mortality in patients with coronary artery disease. *Am. J. Clin. Nutr.* **116**, 1070–1077 (2022).
69. Yu, E. et al. Increases in plasma tryptophan are inversely associated with incident cardiovascular disease in the Prevención con Dieta Mediterránea (PREDIMED) study. *J. Nutr.* **147**, 314–322 (2017).
70. Murr, C. et al. Low serum tryptophan predicts higher mortality in cardiovascular disease. *Eur. J. Clin. Invest* **45**, 247–254 (2015).
71. Qiu, H. et al. Efferocytosis: an accomplice of cancer immune escape. *Biomed. Pharmacother.* **167**, 115540 (2023).
72. Werfel, T. A. et al. Treatment-induced tumor cell apoptosis and secondary necrosis drive tumor progression in the residual tumor microenvironment through MerTK and IDO1. *Cancer Res.* **79**, 171–182 (2019).
73. Wetzel, L. A., Hurtado, M., MacDowell Kaswan, Z. A., McCusker, R. H. & Steelman, A. J. Deletion of indoleamine 2,3 dioxygenase (Ido)1 but not Ido2 exacerbates disease symptoms of MOG(35-55)-induced experimental autoimmune encephalomyelitis. *Brain Behav. Immun. Health* **7**, 100116 (2020).
74. Wang, Y. et al. Mitochondrial fission promotes the continued clearance of apoptotic cells by macrophages. *Cell* **171**, 331–345 (2017).
75. Zhu, W. et al. Quantitative profiling of tryptophan metabolites in serum, urine, and cell culture supernatants by liquid chromatography-tandem mass spectrometry. *Anal. Bioanal. Chem.* **401**, 3249–3261 (2011).
76. Schilperoort, M., Ngai, D., Katerelos, M., Power, D. A. & Tabas, I. PFKFB2-mediated glycolysis promotes lactate-driven continual efferocytosis by macrophages. *Nat. Metab.* **5**, 431–444 (2023).
77. Ngai, D., Schilperoort, M. & Tabas, I. Efferocytosis-induced lactate enables the proliferation of pro-resolving macrophages to mediate tissue repair. *Nat. Metab.* **5**, 2206–2219 (2023).

Acknowledgements

We thank R. Ramakrishnan (Columbia University) for his guidance on statistical analysis of the data in this study. We thank B. Gerlach for his invaluable initial discussions, which greatly contributed to the development of this research. This work was supported by NIH/NHLBI grant nos. R35-HL145228 and P01-HL087123 (to I.T.) and R01-HL159012 (to J.S. and I.T.). D.N. was supported by American Heart Association postdoctoral award no. 24POST1192241. Immunofluorescence imaging experiments were conducted in the Columbia Center for Translational Immunology Core Facility, funded by NIH grant nos. P30CA013696, S10RR027050 and S10OD020056. Flow cytometry experiments were conducted using the Herbert Irving Comprehensive Cancer Center Flow Cytometry Shared Resources, funded in part through NIH grant no. P30CA013696. Samples for histological analysis were prepared in the Molecular Pathology Shared Resource of the Herbert Irving Comprehensive Cancer Center at Columbia University, supported by NIH grant no. P30CA013696. The confocal microscopy work in this study was conducted in the Confocal and Specialized Microscopy Shared Resource of the Herbert Irving Comprehensive Cancer Center at Columbia University, supported by NIH grants nos. P30CA013696 and S10RR025686. This work was supported in part by the Proteomics & Metabolomics Core at Moffitt Cancer Center and funded as part of an NCI-designated Comprehensive Cancer Center (P30 CA076292).

Author contributions

S.R.S. and I.T. conceived the project. P.B.A., D.N., X.W., J.S. and R.H.M. provided additional intellectual input in the development of the project. L.N.F.D. conducted the LC–MS analyses under the guidance of J.M.K. G.K. and Y.X. helped with the mouse atherosclerosis experiments. S.R.S. and I.T. wrote the manuscript and the other co-authors provided comments and revisions.

Competing interests

The authors declare no competing interests.

Additional information

Extended data is available for this paper at https://doi.org/10.1038/s42255-024-01115-7.

Supplementary information The online version contains supplementary material available at https://doi.org/10.1038/s42255-024-01115-7.

Correspondence and requests for materials should be addressed to Santosh R. Sukka or Ira Tabas.

Peer review information *Nature Metabolism* thanks Derek W. Gilroy, Laurent Yvan-Charvet and the other, anonymous, reviewer(s) for their contribution to the peer review of this work. Primary Handling Editor: Alfredo Giménez-Cassina in collaboration with the *Nature Metabolism* team.

https://doi.org/10.1038/s42255-024-01115-7

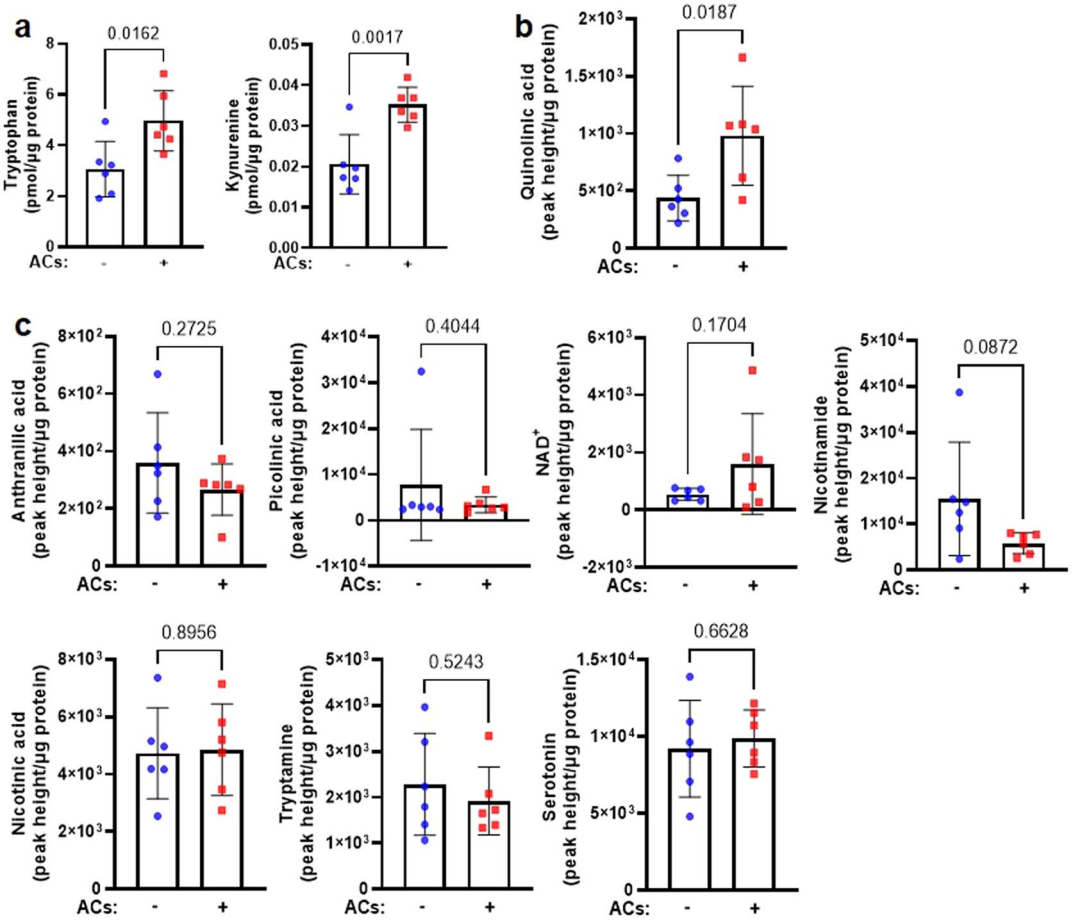

Extended Data Fig. 1 | Related to Fig. 1: Macrophage efferocytosis drives Trp metabolism. a, Tryptophan and kynurenine content expressed as pmol/µg cell protein in BMDMs incubated ± ACs from the experiment in Fig. 1a ($n = 6$ biological replicates/group). **b,c**, Additional metabolite values from BMDMs incubated ± ACs from the experiment in Fig. 1a ($n = 6$ biological replicates/group). Data are mean ± SEM, and significance was determined by two-tailed Student's t-test.

https://doi.org/10.1038/s42255-024-01115-7

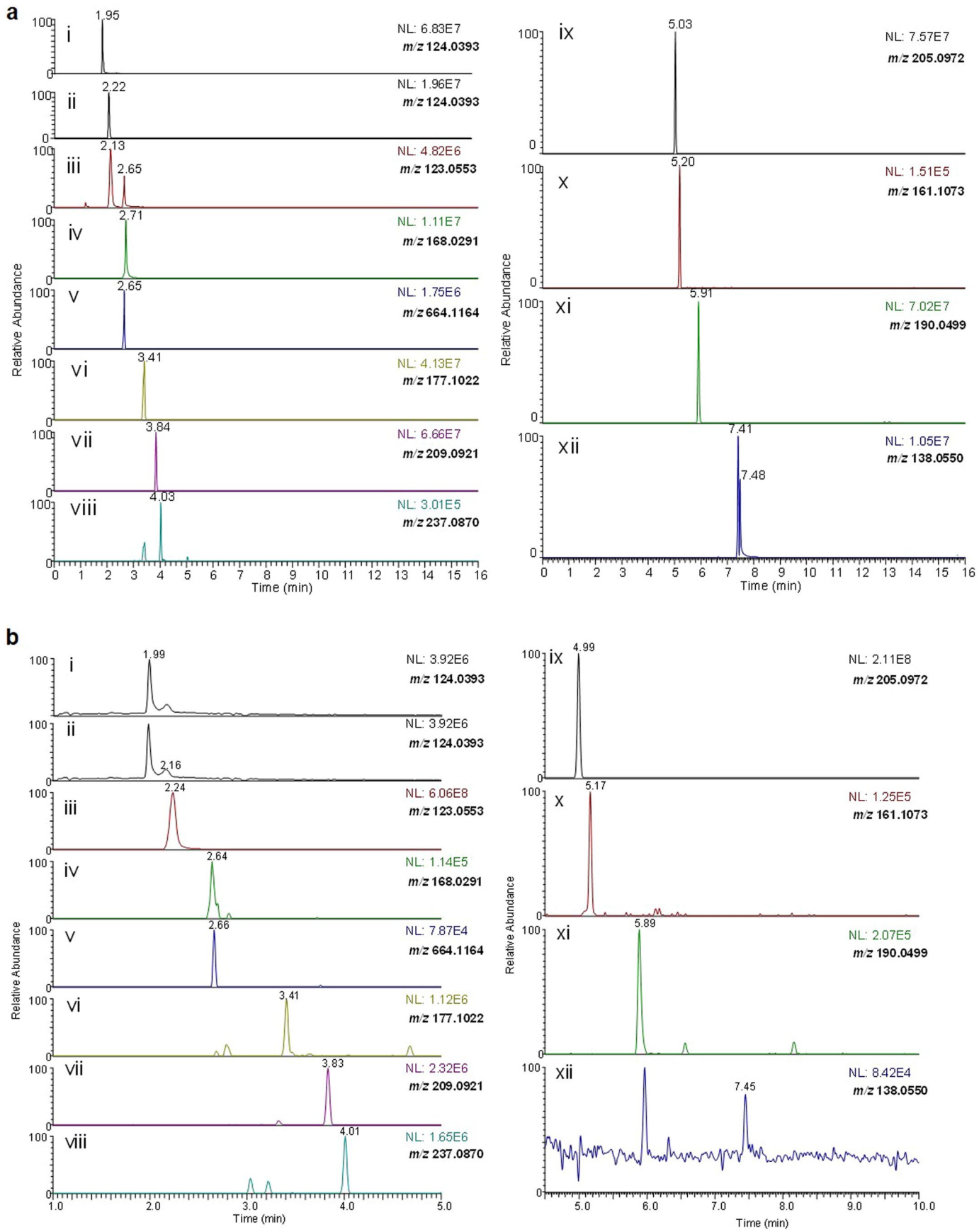

Extended Data Fig. 2 | See next page for caption.

https://doi.org/10.1038/s42255-024-01115-7

Extended Data Fig. 2 | Related to Fig. 1: Examples of extracted ion chromatograms. a, Reversed phase separation and mass spectrometry detection of 12 neat tryptophan metabolite standards (10 ng) individually analyzed. Each trace shows ion signal at a given mass-to-charge ratio (m/z) as the compounds elute from the Atlantis T3 reversed phase column. **b**, Reversed phase separation on an Atlantis T3 reversed phase column and mass spectrometry detection of tryptophan metabolites from an AC- wild type sample. Each trace shows ion signal at a given mass-to-charge ratio (m/z) with a mass tolerance of 5 ppm. For both sets of chromatograms, data are shown for: (**i**) 2^{-}picolinic acid), (**ii**) nicotinic acid, (**iii**) nicotinamide, (**iv**) quinolinic acid, (**v**) nicotinamide adenine dinucleotide (NAD)+, (**vi**) serotonin, (**vii**) DL-kynurenine, (**viii**) N-formylkynurenine, (**ix**) L-tryptophan, (**x**) tryptamine, (**xi**) kynurenic acid, and (**xii**) anthranilic acid. The normalization level (NL) indicates the intensity of the base peak for each spectrum. In b, although more background was observed in the extracted ion chromatogram for anthranilic acid, the anthranilic acid signal is easily differentiated from the background.

https://doi.org/10.1038/s42255-024-01115-7

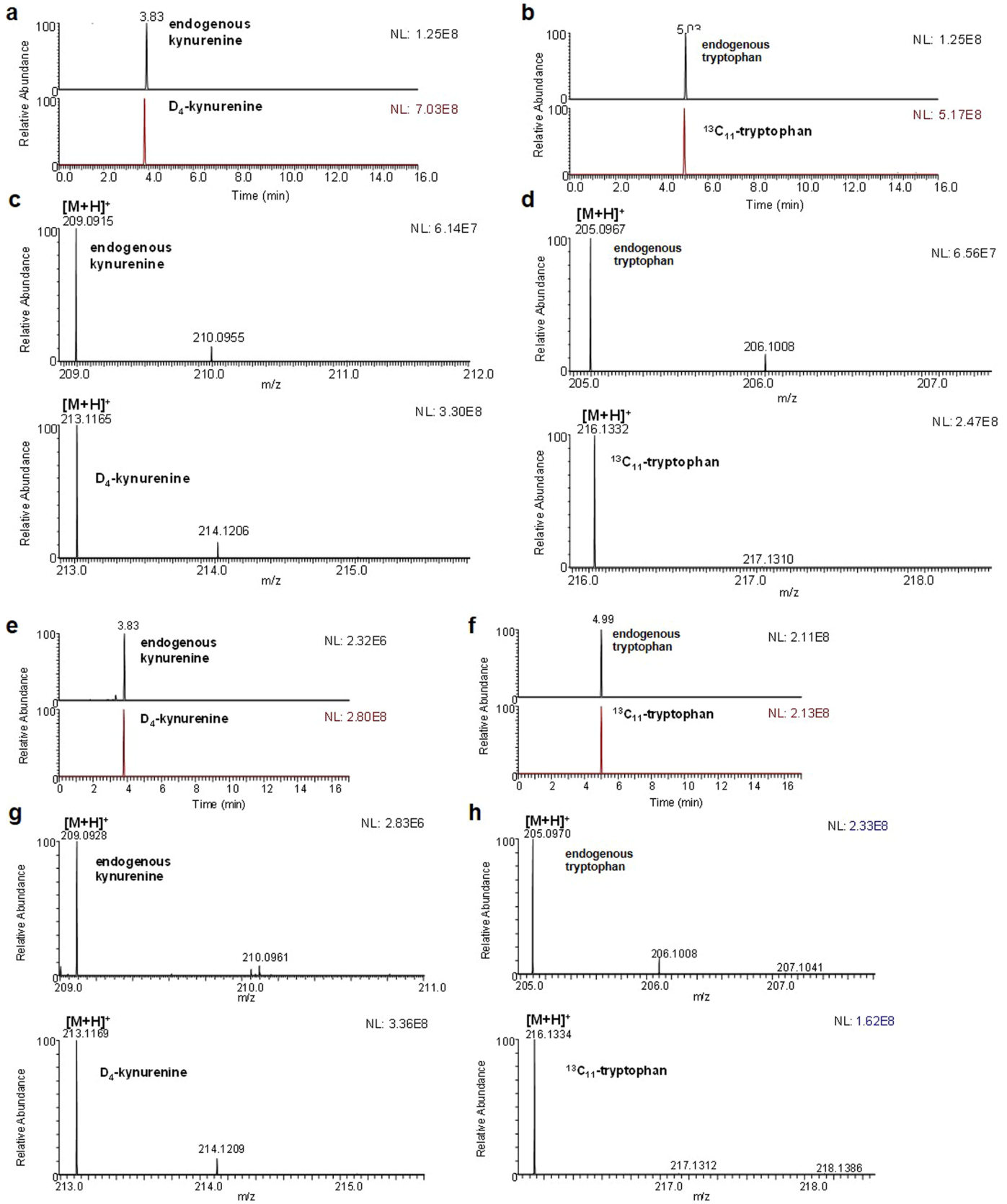

Extended Data Fig. 3 | See next page for caption.

https://doi.org/10.1038/s42255-024-01115-7

Extended Data Fig. 3 | Related to Fig. 1: Absolute quantitation of kynurenine and tryptophan. a-d, Quantitation using a known amount of isotope-labeled standards. **a,b**, Examples of extracted ion chromatograms showing reversed phase separation and mass spectrometry detection for kynurenine (10 ng) and D_4-kynurenine (50 ng); and tryptophan (10 ng) and $^{13}C_{11}$-tryptophan (50 ng). Each trace shows the ion signal at a given mass-to-charge ratio (m/z) as the compounds elute from an Atlantis T3 reversed phase column. **c,d**, Positive ion mass spectra of kynurenine and D_4-kynurenine; and tryptophan and $^{13}C_{11}$-tryptophan. **e-h**, Quantitation of kynurenine and tryptophan in an AC^- wild type sample. **e,f**, Examples of extracted ion chromatograms showing reversed phase separation and mass spectrometry detection for endogenous kynurenine and spiked D_4-kynurenine (50 ng); and endogenous tryptophan and spiked $^{13}C_{11}$-tryptophan (50 ng). Each trace shows the ion signal at a given mass-to-charge ratio (m/z) as the compounds elute from an Atlantis T3 reversed phase column. **g,h**, Positive ion mass spectra of endogenous kynurenine and D_4-kynurenine; and endogenous tryptophan and $^{13}C_{11}$-tryptophan. The normalization level (NL) indicates the intensity of the base peak for each spectrum.

https://doi.org/10.1038/s42255-024-01115-7

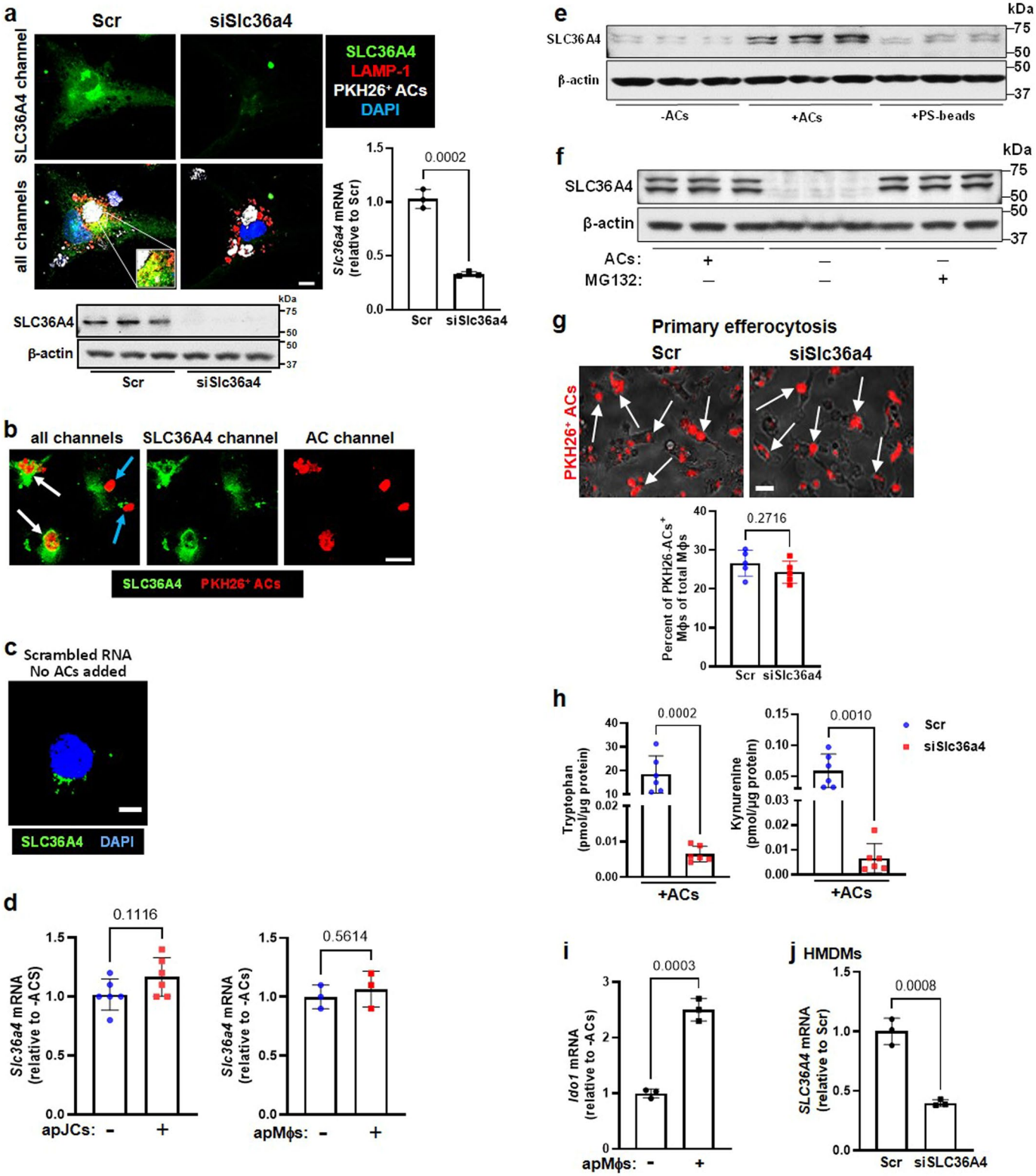

Extended Data Fig. 4 | See next page for caption.

https://doi.org/10.1038/s42255-024-01115-7

Extended Data Fig. 4 | Related to Fig. 1: The role of SLC36A4 in Trp metabolism in efferocytosing macrophages. a, Immunofluorescence microscopy of SLC36A4 (green) and LAMP-1 (red) in Scr- or siSlc36a4-transfected BMDMs incubated 45 mins with PKH26-labelled ACs (pseudocolored white); DAPI (blue) nuclear stain. Scale bar, 50 µm. Another set of cells was assayed for *Slc36a4* mRNA and immunoblotted for SLC36A4 ($n = 3$ biological replicates/group). **b**, Immunofluorescence microscopy of SLC36A4 (green) in BMDMs incubated with PKH26-labelled ACs (red) for 45 min. Scale bar, 50 µm. *White arrows*, engulfed ACs; *blue arrows*, unengulfed ACs. **c**, Representative image of Scr-transfected macrophages not incubated with ACs and then stained for SLC36A4 (green) and DAPI (blue); note low expression of SLC36A4 compared with AC^+ macrophages in Fig. 1b. Image is representative of 3 biological triplicates. Scale bar, 50 µm. **d**, BMDMs were incubated ± apoptotic Jurkat cells (apJCs) or apoptotic macrophages (apMϕs), chased for 3 h, and assayed for *Slc36a4* ($n = 6$ biological replicates/group). **e**, BMDMs were incubated ± ACs or PS-beads for 1 h, chased for 3 h, and immunoblotted for SLC36A4. **f**, BMDMs pre-treated with ± 20 µM MG132 were incubated ± ACs for 1 h, chased for 3 h, and immunoblotted for SLC36A4. **g**, Scr- or siSlc36a4-transfected BMDMs were incubated with PKH26-labelled ACs (red) and quantified for the percentage of $PKH26^+$ macrophages (*arrows*) of total macrophages. Scale bar, 50 µm ($n = 5$ biological replicates/group). **h**, Tryptophan and kynurenine in Scr- or siSlc36a4-transfected BMDMs incubated with ACs (see Fig. 1d; $n = 6$ biological replicates/group). **i**, BMDMs were incubated ± apoptotic macrophages for 1 h and assayed for *Ido1* ($n = 3$ biological replicates/group). **j**, Scr- or siSLC36A4-transfected HMDMs were for *SLC36A4* ($n = 3$ biological replicates/group). All mRNA data are expressed relative to the indicated control groups. Data are mean ± SEM, and significance was determined by two-tailed Student's t-test or one-way ANOVA with Fisher's LSD post-hoc analysis.

https://doi.org/10.1038/s42255-024-01115-7

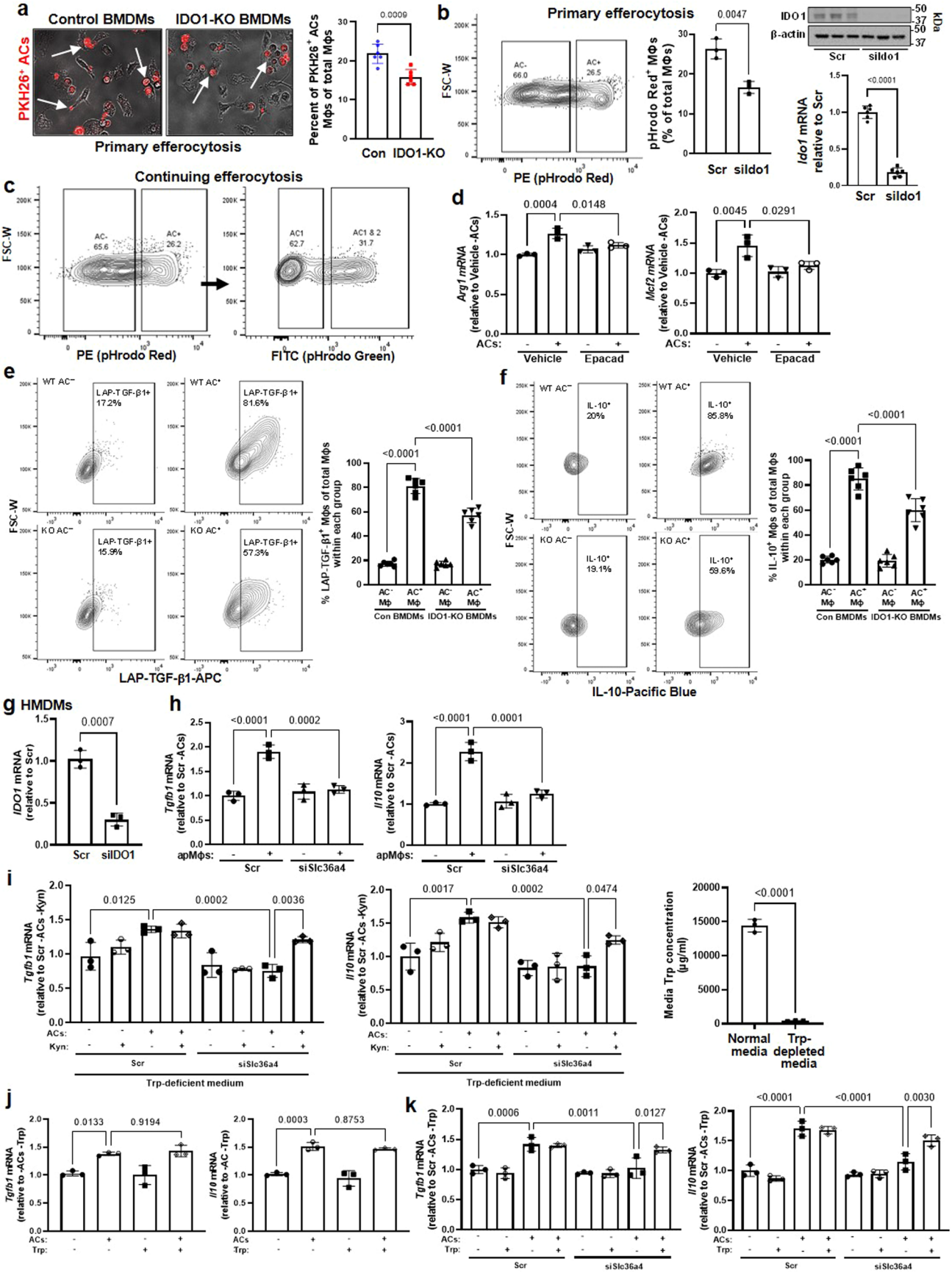

Extended Data Fig. 5 | See next page for caption.

https://doi.org/10.1038/s42255-024-01115-7

Extended Data Fig. 5 | Related to Figs. 2 and 3: Additional data on the roles of SLC36A4 and IDO1 in resolution. a, Control or IDO1-KO BMDMs incubated with PKH26-labelled ACs were quantified for percent PKH26$^+$ macrophages (*arrows*). Scale bar, 50 µm (*n = 6* biological replicates/group). **b**, Scr- or siIdo1-transfected BMDMs incubated with pHrodo-Red-labelled ACs were quantified for percent pHrodo-Red$^+$ macrophages of total macrophages by flow cytometry (*n = 3* biological replicates/group); immunoblotted for IDO1 (*n = 3* samples/group); and assayed for *Ido1* (*n = 6* biological replicates/group). **c**, Flow cytometry contour plots for the experiment in Fig. 2b. **d**, BMDMs treated with ACs ± epacadostat were assayed for *Arg1* and *Mcf2* after a 6-h or 2-h chase, respectively (*n* = 3 biological replicates/group). **e,f**, Contour plots for the experiments in Fig. 2g, h. **g**, Scr- or siIDO1-transfected HMDMs were assayed for *IDO1* (*n = 3* biological replicates/group). **h**, Scr- or siSlc36a4-transfected BMDMs were incubated ± apoptotic macrophages, chased for 6 h, and assayed for *Tgfb1* and *Il10* (*n = 3* biological replicates/group). **i**, Scr- or siSlc36a4-transfected BMDMs were pre-treated ± kynurenine and then incubated ± ACs for 1 h, chased for 6 h in Trp-deficient medium, and assayed for *Tgfb1* and *Il10* mRNA. Right, normal and Trp-depleted media were assayed for Trp by LC$^-$MS/MS (*right*) (*n = 3* biological replicates/group). **j**, BMDMs pre-treated for 1 h with vehicle or 50 µM Trp were incubated ± ACs, chased for 6 h, and assayed for *Tgfb1* and *Il10* (*n = 3* biological replicates/group). **k**, Scr- or siSlc36a4-transfected BMDMs were pre-treated ± 50 µM Trp for 1 h, incubated ± ACs. and assayed for *Tgfb1* and *Il10* (*n = 3* biological replicates/group). All mRNA data are expressed relative to the indicated control groups. Data are mean ± SEM, and significance was determined by two-tailed Student's t-test or one-way ANOVA with Fisher's LSD post-hoc analysis.

https://doi.org/10.1038/s42255-024-01115-7

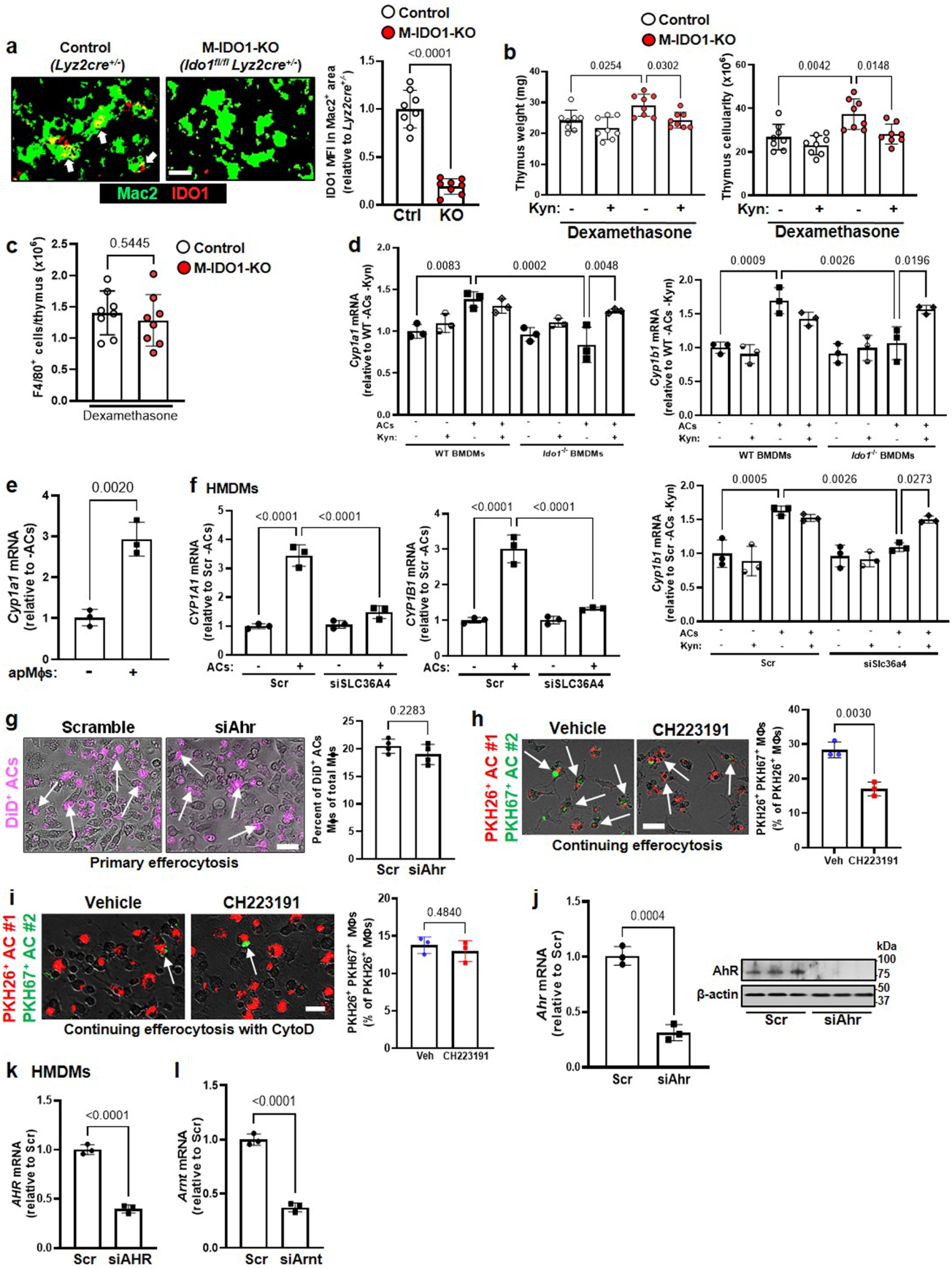

Extended Data Fig. 6 | See next page for caption.

https://doi.org/10.1038/s42255-024-01115-7

Extended Data Fig. 6 | Related to Figs. 4 and 5: Additional in-vivo and in-vitro data on the IDO1-Kyn-AhR pathway. a-c, The thymi of the mice from Fig. 4g–e were immunostained for IDO1 (red) and Mac2 (green) and quantified for IDO1 MFI in $Mac2^+$ areas (*arrows*). Also shown are thymus weight, thymus cellularity, and $F4/80^+$ macrophages/thymus ($n = 8$ mice/group). **d**, Control and $Ido1^{-/-}$ BMDMs (*top 2 graphs*), or Scr- and siSlc364-transfected BMDMs (*bottom graph*), were pre-treated for 1 h ± Kyn and incubated ± ACs. After a 6-h chase, the cells were assayed for *Cyp1a1* and *Cyp1b1* ($n = 3$ biological replicates/group). **e**, BMDMs were incubated ± apoptotic macrophages and assayed for *Cyp1a1*. **f**, Scr- or siSLC36A4-transfected HMDMs were incubated ± ACs, chased for 3 h, and assayed for *CYP1A1* and *CYP1B1* ($n = 3$ biological replicates/group). **g**, Scr- or siAhr-transfected BMDMs were incubated with DiD-labelled ACs and quantified for percent DiD^+ macrophages (*arrows*). Scale bar, 50 µm ($n = 4$ biological replicates/group). **h**, BMDMs pre-treated ± CH223191 were assayed for continuing efferocytosis as in Fig. 2a. *Arrows*, $PKH26^+PKH67^+$ macrophages. Scale bar, 50 µm ($n = 3$ biological replicates/group). **i**, As in panel h, but one of the cohorts was also treated with cytochalasin D before the second round of efferocytosis. *Arrows*, $PKH26^+PKH67^+$ macrophages. Scale bar, 50 µm ($n = 3$ biological replicates/group). **j**, Scr- or siAhr-transfected BMDMs were assayed for *Ahr* ($n = 3$ biological replicates/group) and immunoblotted for AhR protein ($n = 3$ samples/group). **k**, Scr- or siAHR-transfected HMDMs were assayed for *AHR* ($n = 3$ biological replicates/group). **l**, Scr- or siArnt-transfected BMDMs were assayed for *Arnt* ($n = 3$ biological replicates/group). All mRNA data are expressed relative to the indicated control groups. Data are mean ± SEM, and significance was determined by two-tailed Student's t-test or one-way ANOVA with Fisher's LSD post-hoc analysis.

https://doi.org/10.1038/s42255-024-01115-7

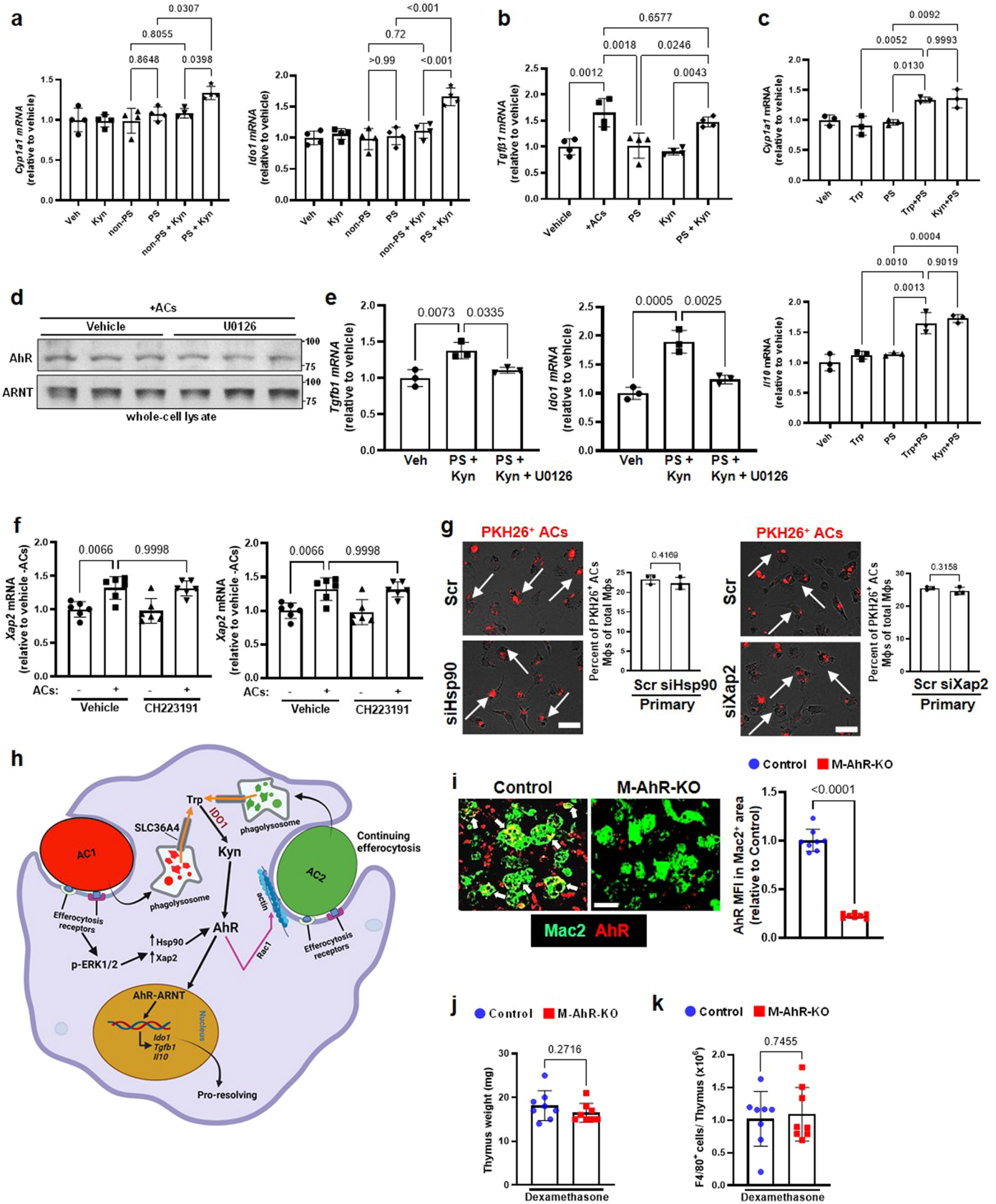

Extended Data Fig. 7 | See next page for caption.

https://doi.org/10.1038/s42255-024-01115-7

Extended Data Fig. 7 | Related to Figs. 6 and 7: Additional in-vivo and in-vitro data on the role of AhR in efferocytosis-induced resolution. a, BMDMs were incubated for 1 h with 100 µM Kyn alone or with control (non-PS) or PS beads ± Kyn and then assayed for *Cyp1a1* and *Ido1* after a 3-h chase ($n = 4$ samples/group). **b**, BMDMs incubated with ACs, PS-beads (PS), Kyn, or PS-beads + Kyn were assayed for *Tgfb1* after a 6-h chase ($n = 4$ samples/group). **c**, BMDMs incubated with 50 µM Trp, PS-beads (PS), Trp and PS-beads, or 100 µM Kyn and PS-beads for 1 h were assayed for *Cyp1a1* and *Il10* after a 3-h or 6-h chase, respectively ($n = 3$ biological replicates/group). **d**, BMDMs pre-treated ± U0126 were incubated with ACs for 1 h and then immunoblotted for AhR and ARNT after a 3-h chase ($n = 3$ samples/group). **e**, BMDMs treated with PS-beads (PS) and Kyn ± U0126 for 1 h were assayed for *Tgfb1* or *Ido1* after a 3-h chase or 6-h chase, respectively ($n = 3$ biological replicates/group). **f**, BMDMs incubated ± ACs ± CH223191 for 1 h were assayed *Hsp90* or *Xap2* after a 3-h chase ($n = 3$ biological replicates/group). **g**, Scr-, siHsp90-, or siXap2-transfected BMDMs were incubated with PKH26-labelled ACs and quantified for percent $PKH26^+$ macrophages (*arrows*). Scale bar, 50 µm ($n = 3$ biological replicates/group). **h**, Proposed pathway (created using BioRender.com): Trp form an efferocytosed AC (AC1) is transported into the macrophage by SLC36A4 and then converted to Kyn by IDO1. Kyn and activated ERK induce Hsp90 and Xap2, leading to AhR-ARNT-mediated transcription of *Tgfb1*, *Il10*, and *Ido1* and Rac1-mediated AC2 internalization (continuing efferocytosis). **i-k**, The thymi of the mice from Fig. 7 were immunostained for AhR (red) and Mac2 (green) and quantified for AhR MFI in $Mac2^+$ areas (*arrows*). Also shown are thymus weight and $F4/80^+$ macrophages/thymus ($n = 8$ mice/group). All mRNA data are expressed relative to the indicated control groups. Data are mean ± SEM, and significance was determined by two-tailed Student's t-test or one-way ANOVA with Fisher's LSD post-hoc analysis.

https://doi.org/10.1038/s42255-024-01115-7

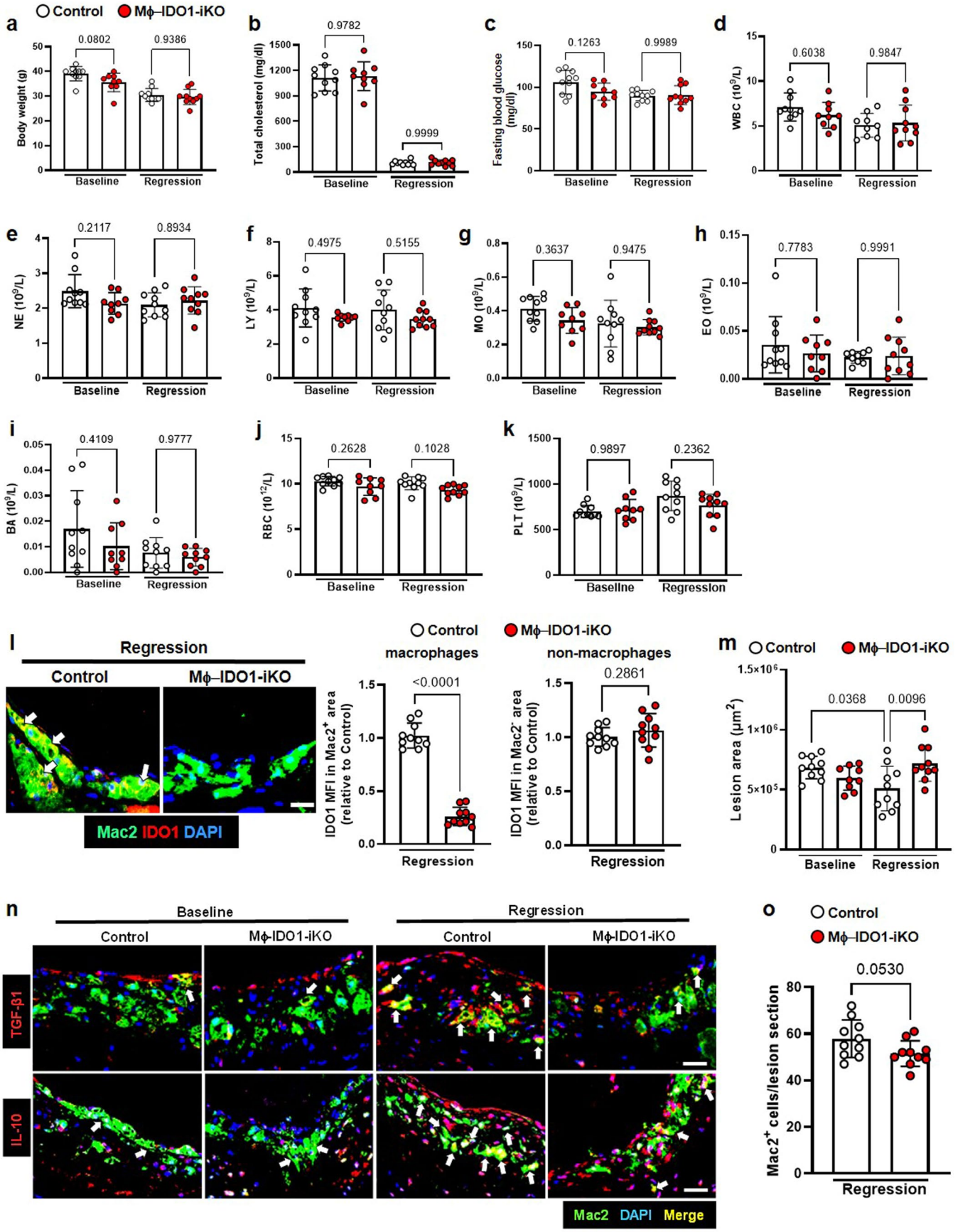

Extended Data Fig. 8 | See next page for caption.

https://doi.org/10.1038/s42255-024-01115-7

Extended Data Fig. 8 | Related to Fig. 8: Systemic and lesional parameters in control and Mϕ-IDO1-iKO BMT *Ldlr*$^{-/-}$ mice. *Ldlr*$^{-/-}$ mice were transplanted with BM from *Ido1*$^{fl/fl}$ (Control) or *Ido1*$^{fl/fl}$*Cx3cr1cre*$^{ERT2+/-}$ (Mϕ-IDO1-iKO) mice and then fed the Western diet for 16 weeks. One cohort from each group was harvested (Baseline), and the rest of the mice were switched to chow diet, injected with HDAd-LDLR virus, and given tamoxifen. After 7 weeks, the mice were harvested (Regression). **a-k**, Body weight, total plasma cholesterol, fasting blood glucose, complete blood count (n = 9–10 mice/group). WBC, white blood cell; NE, neutrophils; LY, lymphocytes; MO, monocytes; EO, eosinophils; BA, basophils, RBC, red blood cells; PLT, platelets. **l**, Immunostaining of IDO1 (red) and Mac2 (green) in regressing aortic root lesions, with quantification of IDO1 MFI in Mac2^{+} and Mac2^{-} areas. *Arrows*, examples of IDO1-Mac2 co-localization. DAPI was used for nuclear staining. Scale bar, 25 µm (n = 10 mice/group). **m**, Quantification of lesion area, based on H&E staining of the aortic root lesions (n = 10 mice/group). **n**, The regressing aortic root lesions of Control and Mϕ-IDO1-iKO groups were immunostained for Mac2 (macrophages; green) and TGF-β1 or IL-10. (red) Arrows, examples of colocalization of Mac2 and TGF-β1 (top) and Mac2 and IL-10 (bottom). DAPI (blue) was used for nuclear staining. Scale bar, 50 µm. **o**, The total number of Mac2^{+} cells per lesion section was quantified in regressing aortic root lesions (n = 10 mice/group). The data are expressed as mean ± SEM, and significance was determined by one-way ANOVA with Fisher's LSD post-hoc analysis for panels a-k and m, and by Student's t-test for panels l and o.

nature portfolio

Corresponding author(s): Dr. Santosh R. Sukka and Dr. Ira Tabas

Last updated by author(s): Jul 12, 2024

Reporting Summary

Nature Portfolio wishes to improve the reproducibility of the work that we publish. This form provides structure for consistency and transparency in reporting. For further information on Nature Portfolio policies, see our Editorial Policies and the Editorial Policy Checklist.

Statistics

For all statistical analyses, confirm that the following items are present in the figure legend, table legend, main text, or Methods section.

n/a	Confirmed	
☐	☒	The exact sample size (*n*) for each experimental group/condition, given as a discrete number and unit of measurement
☐	☒	A statement on whether measurements were taken from distinct samples or whether the same sample was measured repeatedly
☐	☒	The statistical test(s) used AND whether they are one- or two-sided *Only common tests should be described solely by name; describe more complex techniques in the Methods section.*
☒	☐	A description of all covariates tested
☐	☒	A description of any assumptions or corrections, such as tests of normality and adjustment for multiple comparisons
☐	☒	A full description of the statistical parameters including central tendency (e.g. means) or other basic estimates (e.g. regression coefficient) AND variation (e.g. standard deviation) or associated estimates of uncertainty (e.g. confidence intervals)
☐	☒	For null hypothesis testing, the test statistic (e.g. *F*, *t*, *r*) with confidence intervals, effect sizes, degrees of freedom and *P* value noted *Give P values as exact values whenever suitable.*
☒	☐	For Bayesian analysis, information on the choice of priors and Markov chain Monte Carlo settings
☒	☐	For hierarchical and complex designs, identification of the appropriate level for tests and full reporting of outcomes
☒	☐	Estimates of effect sizes (e.g. Cohen's *d*, Pearson's *r*), indicating how they were calculated

Our web collection on statistics for biologists contains articles on many of the points above.

Software and code

Policy information about availability of computer code

Data collection	Profiling of Trp metabolites by LC-MS/MS. FACS Canto was used to collect flow cytometry data. Applied Biosystems 7500 software v. 2.3 was used for qRT-PCR. Leica LAS AF v. 1.9.0 was used to collect epifluorescent microscope images and Nikon A1 was used to collect confocal microscope images.
Data analysis	Peak heights for the Trp and its metabolites as well as the respective stable isotope standards were extracted from the chromatograms using XCalibur Quan Browser version 4.2.47, Thermo Fisher Scientific. ImageJ 2.9.0 was used for analysis of immunofluorescent images. and myImageAnalysis v. 2.0 was used for Western blot densitometry. FlowJo 10.8.1 was used for analysis of flow cytometry data. Statistical analysis was performed using Graph Pad Prism Version 9.4.0.

For manuscripts utilizing custom algorithms or software that are central to the research but not yet described in published literature, software must be made available to editors and reviewers. We strongly encourage code deposition in a community repository (e.g. GitHub). See the Nature Portfolio guidelines for submitting code & software for further information.

Data

Policy information about availability of data

All manuscripts must include a data availability statement. This statement should provide the following information, where applicable:

- Accession codes, unique identifiers, or web links for publicly available datasets
- A description of any restrictions on data availability
- For clinical datasets or third party data, please ensure that the statement adheres to our policy

This study did not generate any unique datasets or codes. All other data can be made available from the authors on reasonable request. Additional data associated with the manuscript can be found in the Supplementary information. Source data are provided within this paper.

Research involving human participants, their data, or biological material

Policy information about studies with human participants or human data. See also policy information about sex, gender (identity/presentation), and sexual orientation and race, ethnicity and racism.

Reporting on sex and gender	Human monocyte-derived macrophages were obtained from the blood collected from anonymous and de-identified adult volunteers (unknown sex and gender).
Reporting on race, ethnicity, or other socially relevant groupings	Unknown (de-identified adult volunteers)
Population characteristics	Unknown (de-identified adult volunteers)
Recruitment	Blood was collected by the New York Blood Center.
Ethics oversight	Blood was collected with informed consent, and the University Institutional Review Board and Health Insurance Portability and Accountability Act guidelines were followed. This is not considered "human research" as it is exempted based on the Protection of Human Rights Title 45 CFR 46.104, section 4 (ii).

Note that full information on the approval of the study protocol must also be provided in the manuscript.

Field-specific reporting

Please select the one below that is the best fit for your research. If you are not sure, read the appropriate sections before making your selection.

☒ Life sciences ☐ Behavioural & social sciences ☐ Ecological, evolutionary & environmental sciences

For a reference copy of the document with all sections, see nature.com/documents/nr-reporting-summary-flat.pdf

Life sciences study design

All studies must disclose on these points even when the disclosure is negative.

Sample size	Previous studies and pilot experiments in the lab form the basis of power calculations for the various studies. Depending on the experiments and power calculations, the number of mice chosen for each cohort was sufficient to ensure the testing of our hypotheses based on an expected 20%–30% coefficient of variations and an 80% probability of identifying a 33% difference in crucial plaque metrics. e.g., fibrous cap thickness and necrotic area.
Data exclusions	Initial exclusion criteria for the in-vivo studies included death, injury requiring euthanasia, or weight loss > 15%, but only one mouse was excluded in this study, which was for injury in the atherosclerosis experiment.
Replication	All experiments were reproducible as assessed by multiple wells of cells, tissues, or mice. For in vitro assays, experiments involved 3 or more biological replicates, and key experiments were repeated multiple times and proved reproducible. For the in vivo study, 5-10 mice were used per group. These numbers produced robust data and sufficient power for statistical analysis.
Randomization	Mice of the same age and similar weight were randomly assigned to experimental and control groups.
Blinding	Investigators were not blinded for in vitro assays and some in vivo experiments for practical reasons (e.g., to apply different treatments such as PBS versus dexamethasone/Zymosan injection in mice) but the primary outcome data (efferocytosis assays and analysis of immunohistochemical and immunofluorescent stainings were confirmed by a blinded second investigator. Investigators were blinded for atherosclerosis lesion and necrotic size quantifications.

Reporting for specific materials, systems and methods

We require information from authors about some types of materials, experimental systems and methods used in many studies. Here, indicate whether each material, system or method listed is relevant to your study. If you are not sure if a list item applies to your research, read the appropriate section before selecting a response.

Materials & experimental systems

n/a	Involved in the study
☐	☒ Antibodies
☐	☒ Eukaryotic cell lines
☒	☐ Palaeontology and archaeology
☐	☒ Animals and other organisms
☒	☐ Clinical data
☒	☐ Dual use research of concern
☒	☐ Plants

Methods

n/a	Involved in the study
☒	☐ ChIP-seq
☐	☒ Flow cytometry
☒	☐ MRI-based neuroimaging

Antibodies

Antibodies used

The source, catalogue number, and vendors of all antibodies that were used in this manuscript can be found in the list below:

Rabbit anti-SLC36A4 pAb (mouse) – Aviva Systems Biology Cat# AAP44114 (1:200 IF, 1:1000 WB)
Rabbit anti-IDO1 mAb (mouse) – Cell Signalling Technology Cat# 51851S, RRID: AB_2799402 (1:200 IF, 1:1000 WB)
Mouse APC (mouse) LAP (TGF-β1) – Biolegend Cat# 141406, RRID: AB_10898159 (1:100 FCM)
Rat PB (mouse) IL-10 – Biolegend Cat# 505020, RRID: AB_2125094 (1:100 FCM)
Rabbit TGFβ1 pAb (mouse) – Abcam Cat# ab92486, RRID: AB_10562492 (1:200 FCM)
Rabbit IL-10 pAb (mouse) – Abcam Cat# ab9969, RRID: AB_308826 (1:200 FCM)
Rat PB (mouse) Ly6G – Biolegend Cat# 127612, RRID: AB_1877212 (1:100 FCM)
FITC anti-annexin V – Biolegend Cat# 640906 (1:50 FCM)
Rabbit anti-AhR pAb (mouse) – Enzo Life Sciences Cat# BML-SA210-0100 (1:50 IP, 1:200 IF, 1:1000 WB)
Rabbit anti-ARNT mAb (mouse) – Cell Signalling Technology Cat# 5537S, RRID: AB_10694232 (1:50 IP, 1:1000 WB)
Rabbit anti-NPM pAb (mouse) – Cell Signalling Technology Cat# 3542S, RRID: AB_2155178 (1:1000 WB)
Rabbit anti-β-actin-HRP mAb (mouse) – Cell Signalling Technology Cat# 5125S (1:5000 WB)
Rabbit anti-p44/42 MAPK (ERK1/2) pAb (mouse) – Cell Signalling Technology Cat# 9102S, RRID: AB_330744 (1:1000 WB)
Rabbit anti-phospho-Thr202/Tyr204-p44/42 MAPK (ERK1/2) mAb (mouse) – Cell Signalling Technology Cat# 4370S, RRID: AB_2315112 (1:1000 WB)
Rat anti-LAMP1 mAb (mouse) – DSHB Cat# 1D4B, RRID: AB_2134500 (1:200 IF)
Rat anti-Mac2 (mouse) – Cedarlane Cat# CL8942AP, RRID: AB_10060357 (1:10000 IF)
Rat PE (mouse) F4/80 – Biolegend Cat# 123110, RRID: AB_893486 (1:100 FCM)
Rabbit anti-IgG mAb (mouse) – Cell Signalling Technology Cat# 3900 (1:250 IP)
Alexa fluor 488 goat anti-rat IgG – Invitrogen Cat# A11006, RRID: AB_2534074 (1:200 IF)
Alexa fluor 594 goat anti-rabbit IgG – Invitrogen Cat# A11037, RRID: AB_2534095 (1:200 dilution)
Alexa fluor 488 goat anti-rabbit IgG – Invitrogen Cat# A11034, RRID: AB_2576217 (1:200 dilution)

Validation

Antibody against SLC36A4 has been validated in the manuscript using siRNA -mediated knockdown strategies (Fig. 1b and Extended Data Fig. 1c).
All of these commercial antibodies have been validated, with proof available through publications or references on the manufacturers' websites, by other researchers, or from data published by lab members as stated on the manufacturers' websites:

Rabbit anti-SLC36A4 pAb (mouse) – Aviva Systems Biology Cat# AAP44114 - validated for WB by Aviva Systems Biology and 1 product reference; and IF in this manuscript.
Rabbit anti-IDO1 mAb (mouse) – CST Cat# 51851S - validated for WB & IF by CST, 13 product references and in this manuscript.
Mouse APC (mouse) LAP (TGF-β1) – Biolegend Cat# 141406 - validated for FC by Biolegend, 20 product references and in this manuscript.
Rat PB (mouse) IL-10 – Biolegend Cat# 505020 - validated for FC by Biolegend, 2 product references and in this manuscript.
Rabbit TGFβ1 pAb (mouse) – Abcam Cat# ab92486 - validated for IF by Abcam, 9 product references and in this manuscript.
Rabbit IL-10 pAb (mouse) – Abcam Cat# ab9969 - validated for IF by Abcam, 10 product references and in this manuscript.
Rat PB (mouse) Ly6G – Biolegend Cat# 127612 - validated for FC by Biolegend, 27 product references and in this manuscript.
FITC anti-annexin V – Biolegend Cat# 640906 - validated for FC by Biolegend, 243 product references and in this manuscript.
Rabbit anti-AhR pAb (mouse) – Enzo Life Sciences Cat# BML-SA210-0100 - validated for WB by Enzo Life Sciences and 6 product reference; and WB & IF in this manuscript.
Rabbit anti-ARNT mAb (mouse) – CST Cat# 5537S - validated for IP by CST, 77 product references and in this manuscript.
Rabbit anti-NPM pAb (mouse) – CST Cat# 3542S - validated for WB by CST, 67 product references and in this manuscript.
Rabbit anti-β-actin-HRP mAb (mouse) – CST Cat# 5125S - validated for WB by CST, 503 product references and in this manuscript.
Rabbit anti-p44/42 MAPK (ERK1/2) pAb (mouse) – CST Cat# 9102S - validated for WB by CST, 7533 product references and in this manuscript.
Rabbit anti-phospho-Thr202/Tyr204-p44/42 MAPK (ERK1/2) mAb (mouse) – CST Cat# 4370S - validated for WB by CST, 7533 product references and in this manuscript.
Rat anti-LAMP1 mAb (mouse) – DSHB Cat# 1D4B - validated for IF by DSHB, 56 product references and in this manuscript.
Rabbit anti-IgG mAb (mouse) – CST Cat# 3900 - validated for WB by CST, 713 product references and in this manuscript.

Rat PE (mouse) F4/80 – Biolegend Cat# 123110 - validated for FC by Biolegend, 345 product references and in this manuscript.
Rat anti-Mac2 (mouse) – Cedarlane Cat# CL8942AP - validated for IF by Cedarlane, 213 product references and in this manuscript.
Alexa fluor 488 goat anti-rat IgG – Invitrogen Cat# A11006 - validated for IF by Invitrogen, 2134 product references and in this manuscript.
Alexa fluor 594 goat anti-rabbit IgG – Invitrogen Cat# A11037 - validated for IF by Invitrogen, 2186 product references and in this manuscript.
Alexa fluor 488 goat anti-rabbit IgG – Invitrogen Cat# A11034 - validated for IF by Invitrogen, 6842 product references and in this manuscript.

Eukaryotic cell lines

Policy information about cell lines and Sex and Gender in Research

Cell line source(s)	Human Jurkat T Lymphocyte-ATCC TIB-152 and L-929 mouse fibroblasts (ATCC CCL-1)
Authentication	None of the cell lines used were authenticated.
Mycoplasma contamination	Not tested for the mycoplasma contamination
Commonly misidentified lines (See ICLAC register)	No commonly misidentified cell lines were used in this study.

Animals and other research organisms

Policy information about studies involving animals; ARRIVE guidelines recommended for reporting animal research, and Sex and Gender in Research

Laboratory animals	The mice were housed in standard cages at room temperature with a 12-h light/12-h dark cycle in a barrier facility with ad libitum access to water and food. Male C57BL/6J wild-type mice (8-10-week-old) were purchased from The Jackson Laboratory (strain #000664) were used as bone marrow transplant (BMT)-recipient mice for the zymosan A1 and dexamethasone-thymus experiments. Male Ldlr-/- mice (8-10-week-old) mice on the C57BL/6J background (B6.129S7-Ldlrtm1Her/J; Jackson Laboratory, strain #002207) were used as BMT-recipient mice for the atherosclerosis experiments. All purchased mice were allowed to adapt to housing in the animal facility for 1 week before the commencement of experiments. For BMT donor mice, we used 8-10-week-old Lyz2cre+/– (Control) and Ido1fl/fl Lyz2cre+/– (M-IDO1-KO) male mice, both on the C57BL/6J background. Lyz2Cre mice were purchased from The Jackson Laboratory (strain # 004781). Ahrfl/fl mice were purchased from The Jackson Laboratory (strain #006203). Ido1fl/fl Cx3cr1creERT2 mice were bred using Cx3cr1creERT2 mice purchased from The Jackson Laboratory (strain #020940).
Wild animals	No wild animals were used in this study
Reporting on sex	Only male mice from Jackson Laboratory were used for the studies in this manuscript.
Field-collected samples	No field-collected samples were used in this study.
Ethics oversight	The mouse protocols used for experiments were approved by Columbia University's Institutional Animal Care and Use Committee, and the mice were cared for according to National Institutes of Health (NIH) guidelines for the care and use of laboratory animals.

Note that full information on the approval of the study protocol must also be provided in the manuscript.

Plants

Seed stocks	*Report on the source of all seed stocks or other plant material used. If applicable, state the seed stock centre and catalogue number. If plant specimens were collected from the field, describe the collection location, date and sampling procedures.*
Novel plant genotypes	*Describe the methods by which all novel plant genotypes were produced. This includes those generated by transgenic approaches, gene editing, chemical/radiation-based mutagenesis and hybridization. For transgenic lines, describe the transformation method, the number of independent lines analyzed and the generation upon which experiments were performed. For gene-edited lines, describe the editor used, the endogenous sequence targeted for editing, the targeting guide RNA sequence (if applicable) and how the editor was applied.*
Authentication	*Describe any authentication procedures for each seed stock used or novel genotype generated. Describe any experiments used to assess the effect of a mutation and, where applicable, how potential secondary effects (e.g. second site T-DNA insertions, mosiacism, off-target gene editing) were examined.*

Flow Cytometry

Plots

Confirm that:

☒ The axis labels state the marker and fluorochrome used (e.g. CD4-FITC).

☒ The axis scales are clearly visible. Include numbers along axes only for bottom left plot of group (a 'group' is an analysis of identical markers).

☒ All plots are contour plots with outliers or pseudocolor plots.

☒ A numerical value for number of cells or percentage (with statistics) is provided.

Methodology

Sample preparation	After fixation in 4% PFA (Thermo Fisher Scientific), cells were resuspended in FACS staining buffer (BioLegend)) and incubated with mouse TruStain FcXTM PLUS (CD16/32, Biolegend) Fc-blocking antibody (Biolegend). Cell-surface receptor staining was carried out by incubating the cells with fluorescent antibodies for 1 h at 4°C. Cells were permeabilized with BD Perm/Wash (BD Biosciences) for intracellular staining, followed by incubation with fluorescent antibodies for 1 h at 4°C. Subsequently, cells were washed in FACS buffer (twice) and then resuspended for analysis on a BD FACS Canto II flow cytometer. For apoptosis detection, cells were washed with cold FACS buffer (twice), resuspended in annexin V-binding buffer at a concentration of 1 × 10^6 cells per ml, and incubated with fluorescein isothiocyanate (FITC)-conjugated annexin V antibody for 15-20 min at room temperature. The samples were then analysed by a BD FACS Canto II flow cytometer.
Instrument	BD FACS Canto II flow cytometer
Software	Data analysis was carried out using the FlowJo_10.8.1.
Cell population abundance	No sorting was done.
Gating strategy	FSC-A/SSC-A gating was used to detect all events. FSC-A/FSC-W was used to select singlets.

☒ Tick this box to confirm that a figure exemplifying the gating strategy is provided in the Supplementary Information.